Paleowildfire at the end-Triassic mass extinction: smoke or fire?

Calum P. Fox[1,2,#], Alex I. Holman[1], Manuel Rigo[3,4], Aisha Al Suwaidi[2], Kliti Grice[1]

[1]WA Organic & Isotope Geochemistry Centre, The Institute of Geoscience Research, School of Earth and Planetary Sciences, Curtin University, Bentley, WA 6102, Australia

[2]Department of Earth Sciences, Khalifa University of Science and Technology, PO BOX 127788, Abu Dhabi, United Arab Emirates

[3]Department of Geosciences, Università degli Studi di Padova, 35131 Padova, Italy

[4]IGG – CNR, Via G. Gradenigo 6, 35131 Padova, Italy

[#]calum.fox@ku.ac.ae; calum_fox@hotmail.co.uk

Abbreviations (as they appear in text):

ETE – end-Triassic mass extinction

CIE – Carbon isotope excursion

PAH_{PCD} – Potentially combustion-derived polycyclic aromatic hydrocarbons

IP/IP+BghiP – indeno[1,2,3-cd]pyrene/indeno[1,2,3-cd]pyrene + benzo[*ghi*]perylene

BaP/BaP+C&T – benzo[*a*]anthracene/benzo[*a*]anthracene + chrysene and triphenylene

1,7/1,7+2,6 DMP – 1,7 dimethylphenanthrene/1,7 + 2,6 dimethylphenanthrene

1-+2-MP/P – (1- + 2-methylphenanthrene)/phenanthrene

Fl/Fl+Py – fluoranthene/fluoranthene + pyrene

Abstract

Polycyclic Aromatic Hydrocarbons (PAHs) are routinely used as proxies for wildfire in geological sediments associated with large igneous province (LIP) driven CO_2 increases and mass extinction events. One example is the end-Triassic mass extinction event (ETE) driven by Earth's most laterally extensive LIP, the Central Atlantic Magmatic Province (CAMP). However, many PAH records often lack critical information including identifying specific source(s) of PAHs (e.g., pyrogenic vs. petrogenic), intensity of paleowildfire events, whether PAHs represent predominant smoke signals that can travel substantial distance from the burn origin, and if evidence of PAH as markers for soil erosion exists. To better understand ETE wildfire events, a detailed evaluation of PAH distributions from the Italcementi section in the Lombardy Basin, Italy covering the latest Rhaetian was undertaken. We report the best evidence of wildfire activity occurs above the initial carbon isotope excursion (CIE) which is routinely used to chemostratigraphically correlate between ETE sections, rather than within the initial CIE as evidenced at other sections. This wildfire event was intense, short-lived, and occurred during a calcification crisis and $\delta^{13}C_{org}$ anomaly, thereby linking terrestrial and marine ecosystem stress. Evidence of a more prolonged but less intense wildfire event and/or evidence for smoke signals takes place above this interval before the onset of a second calcification crisis. By comparing PAH records from Italy, Greenland, Poland, the UK, and China, during the ETE, few sections show evidence for intense (i.e., higher-temperature) wildfire activity during the initial CIE. However, these investigated PAH records show prolonged increases in the low-molecular-weight (LMW) combustion-derived PAH phenanthrene. We interpret this to represent widespread (and possibly more intense) wildfire activity further from the deposition sites, since LMW combustion-derived PAHs are the major PAHs in smoke aerosols that can travel vast distances, and/or less intense wildfire activity that characteristically produce LMW combustion-derived PAHs. In comparing PAH data, we find widespread wildfire activity across multiple basins supporting wildfire activity was an important ecological stressor in the terrestrial realm during the ETE.

Keywords: polycyclic aromatic hydrocarbons; end-Triassic; mass extinction; Central Atlantic Magmatic Province; wildfire; soil erosion

1: Introduction

Earth's history is punctuated by five major extinction events in which loss of life is recorded in marine and terrestrial realms globally over short geological time periods (Sepkoski, 1993). The end-Triassic mass extinction event (ETE) that occurred ~201 Ma (Blackburn et al., 2013) was driven by massive input of pCO_2 and other harmful volatiles from Earth's most laterally extensive large igneous province (LIP), the Central Atlantic Magmatic Province (CAMP) (Davies et al., 2017; Lindström et al., 2021; Schoene et al., 2010; Whiteside et al., 2010). The CAMP-induced doubling to tripling of paleoatmospheric CO_2 concentrations from values between 600-1000 ppm to 2000-2500 ppm (McElwain et al., 1999; Steinthorsdottir et al., 2011) are expected to have led to a series of cascading environmental catastrophes resulting in the ETE (Pálfy, 2003; van de Schootbrugge and Wignall, 2015), although the precise extinction drivers are still under debate.

Although still not completely understood, multiple geochemical proxies illustrate that combinations of acidification, anoxia, and photic zone euxinia (i.e., H_2S poisoning in the sun-lit region of the water column) are important mechanisms of marine extinction for the ETE (Atkinson and Wignall, 2019; Beith et al., 2021; Bond et al., 2022; Fox et al., 2022a, 2020; He et al., 2020; Jaraula et al., 2013; Kasprak et al., 2015; McRoberts et al., 2012; van de Schootbrugge et al., 2013; van de Schootbrugge and Wignall, 2015). Contrastingly the mechanisms responsible for the loss of life on land have received much less attention and are poorly understood. Terrestrial ecological stressors include soil erosion evidenced from reworked pollen and spores across much of Europe (van de Schootbrugge et al., 2020) and abundant polycyclic aromatic hydrocarbons (PAHs) derived from a common lignin source (Fox et al., 2022b and references therein), soil acidification evidenced by darkened palynomorphs (Pieńkowski et al., 2011; van de Schootbrugge et al., 2009), and volcanically-induced mutagenesis of palynomorphs (Lindström et al., 2019). In addition to these ecological stressors, the CAMP is also expected to have driven intensive wildfire activity similar to that evidenced during the end-Permian mass extinction (e.g., Grice et al., 2007; Kaiho et al., 2020; Nabbefeld et al., 2010; Shen et al., 2011) that, supported by recent burning events (e.g., the Australian 2019/2020 bush fires), would have been detrimental to terrestrial organisms. Elevated charcoal abundances and increases in PAHs that can form from the incomplete combustion of organic matter give evidence of ETE paleowildfire events. Currently, charcoal and PAHs that can form from incomplete combustion are identified from basins in Greenland (Belcher et al., 2010; Williford et al., 2014), Europe (Fox et al., 2022b; Harris, 1958; Kaiho et al., 2022; Marynowski

and Simoneit, 2009; Petersen and Lindström, 2012; Uhl and Montenari, 2011), Iran (Alipour et al., 2021), and China (Fang et al., 2021; Pole et al., 2018; Song et al., 2020; Zhang et al., 2020) (Fig. 1). Contrastingly, van de Schootbrugge et al., (2009) suggest increases in PAHs in NW German sections that can form from incomplete combustion are related to CAMP activity, likely CAMP intrusions into organic-matter rich deposits, rather than wildfire activity based on absence of charcoal and PAH profiles differing from modern burn experiments. However, Fox et al., (2022b) argue a wildfire origin cannot be entirely ruled out for such increases based on other and more recent findings that suggest the PAH profiles in NW Germany are consistent with intense burning.

Increases in PAHs that can form from incomplete combustion are commonly used as evidence of paleowildfire activity across the ETE and other periods of LIP-driven global warming (Baker, 2022 and refs therein). However, these PAHs can have other sources and also represent processes unrelated to fire events including volcanic and hydrothermal vent activities (Holman and Grice, 2018; Simoneit et al., 1990) meteorites (Lyons et al., 2020; McKay et al., 1996), tsunamis (Gulick et al., 2019), changes to the hydrological cycle (Finkelstein et al., 2005), helping determine the origin of organic matter (allochthonous versus autochthonous), degree of organic matter degradation (Denis et al., 2021 and refs therein), and input of older possibly soil-derived PAH compounds (Fox et al., 2022b). More recent studies have successfully demonstrated the importance of whether PAHs that can form from incomplete combustion have pyrogenic (i.e., fire-derived) or petrogenic (oil/coal-derived) origins (Fox et al., 2022b; Karp et al., 2018; Song et al., 2020), whether PAHs represent smoke or char/burn residue inputs (Karp et al., 2020), and the intensity of wildfire events (e.g., Kaiho et al., 2020). Since many ETE PAH studies were first presented prior to these findings, they lack these more critical evaluations. Additionally, few ETE PAH studies investigate selected low-molecular-weight (LMW) PAHs (typically defined as PAHs containing 3 or fewer rings; Table 1) that are attributed to processes other than fire, such as soil erosion (Sephton et al., 2005; Wang and Visscher, 2007) and markers of ecosystem collapse (Fenton et al., 2007) that are also crucial to better understanding ETE ecological perturbations.

To better determine the ETE paleowildifre and soil erosion record, we investigated LMW and high molecular-weight (HMW) PAH compounds in the Lombardy Basin, Northern Italy and compare our findings to PAH records reported from globally dispersed sites.

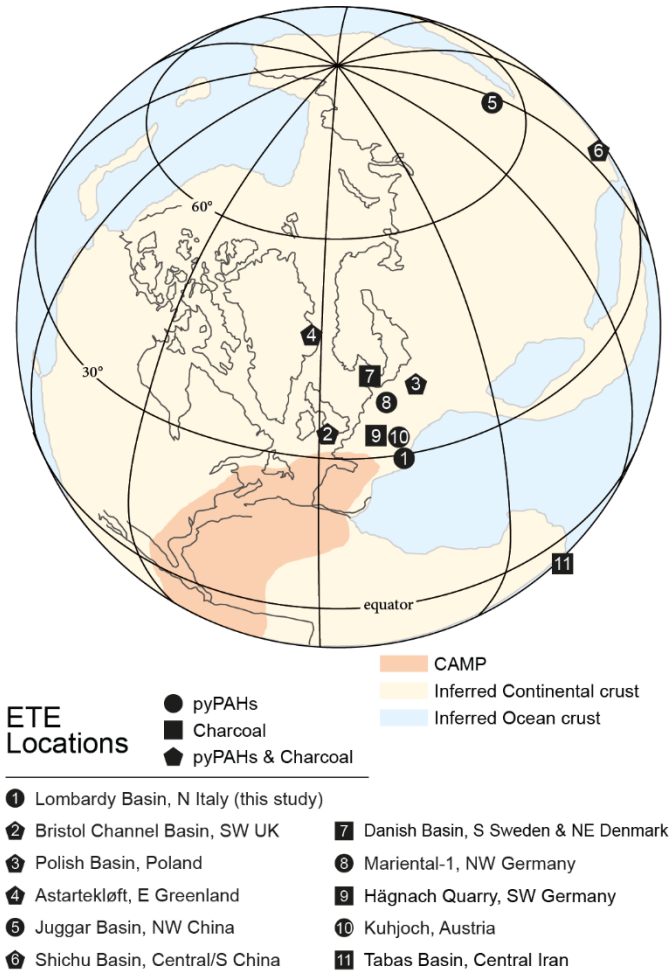

Figure. 1: Paleogeographic reconstruction of the ETE after Fox et al., (2022b) with localities that show evidence of paleowildfire through PAHs, charcoal, or both (Alipour et al., 2021; Fang et al., 2021; Harris, 1958; Kaiho et al., 2022; Marynowski and Simoneit, 2009; Petersen and Lindström, 2012; Pole et al., 2018; Song et al., 2020; Uhl and Montenari, 2011; van de Schootbrugge et al., 2009; Williford et al., 2014; Zhang et al., 2020). PAH profiles from locations 1-6 are summarised in Fig. 6.

2: Studied section and $\delta^{13}C_{org}$ record

The Lombardy Basin in Northern Italy contains strata from the Norian (Triassic) to the earliest Hettangian (Jurassic) and comprises multiple sections including a composite section of the Brumano and Italcementi sections used in this study, which are fully described in Zaffani et al., (2018). These sections contain the Calcare di Zu Formation that is comprised of the Zu 1, Zu 2, and Zu 3 members, with the Zu 3 Member sub dived into the Zu 3a, Zu 3b and Zu 3c

sub-members (Jadoul et al., 1994). Whereas the Brumano section consists of the Zu 1, Zu 2, and Zu 3a members, the Italcementi section contains the Zu 3b and Zu 3c members that are overlain by the Malanotte Formation (Fig. 2). Since these intervals encompass the whole of the Rhaetian and the early Hettangian, samples were analysed from only the Italcementi section that represents the latest Rhaetian (Zu 3b and Zu 3c submembers) and earliest Hettangian (Malanotte Formation). This Basin, with a paleolatitude of ~ 20°N, is representative of the subtropics in the northwest Tethys Ocean (Kent and Muttoni, 2003; Muttoni et al., 2010).

The Zu 3 Member ranges from 120 m to over 200 m in thickness and was deposited on a mid-to-inner carbonate ramp that recorded a transgressive-regressive cycle (Galli et al., 2007; Jadoul et al., 1994). Given that our samples are from only the Zu 3b and Zu 3c members, we describe here lithology and fossil occurrence of these members in detail. For further details of the Lombardy basin see Galli et al., (2007), Jadoul et al., (2007), and Jadoul and Galli, (2008).

The Zu 3b Member consists of alternating grey to greenish marls and micritic limestones that are interbedded with marly limestone and darker marly shales (Galli et al., 2007). There is evidence of storm deposits (iron-rich tempestites) throughout the Member as well as evidence of evaporitic horizons, typically associated with breccia, and stromatolites toward the lower part of the section. These facies are interpreted as a mid-ramp environment (Bottini et al., 2016; Galli et al., 2007; Jadoul et al., 2004). The Zu 3c Member consists of predominantly micritic limestone and calcernite with some darker marly shales (Galli et al., 2007) and marked by increases in biogenic packstone-grainstone (Zaffani et al., 2018). This Member contains evidence of patch-reefs and regional carbonate platform inner ramp progradation. There is more evidence of bioturbation throughout the Member compared to the Zu 3b Member, as well as more evidence of corals. The top of the section is often, but not always, characterized by an Fe hardground and a paraconformity sometimes attributed to the beginning of the ETE that were not observed in the samples analysed in this study (Galli et al., 2007; Zaffani et al., 2018 and refs therein).

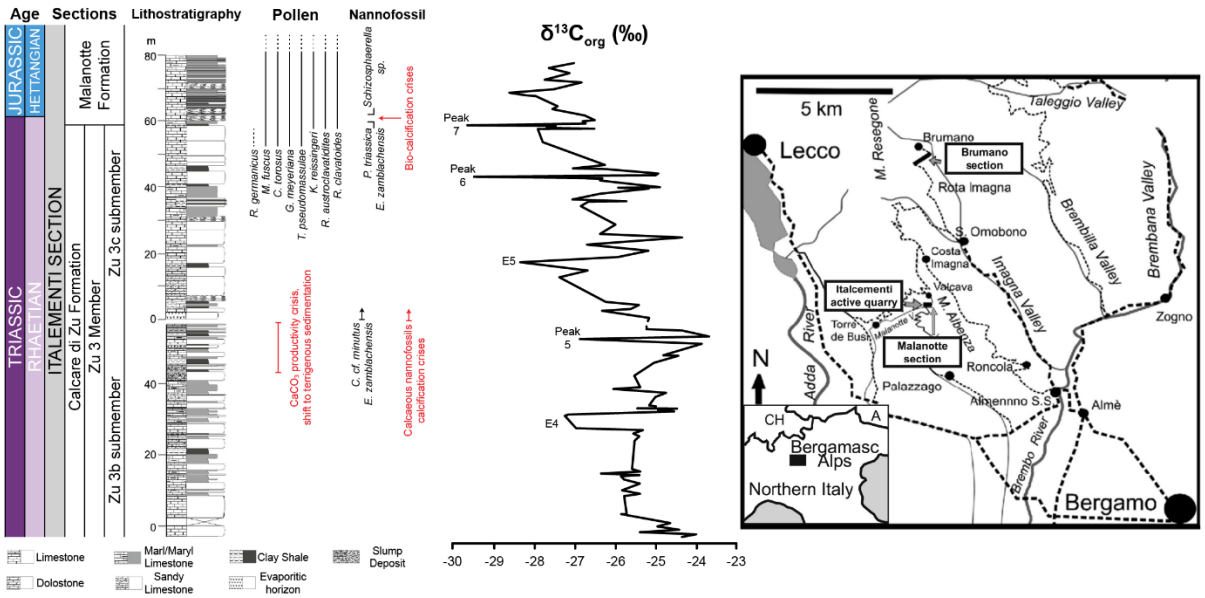

Figure 2: Lithology, $\delta^{13}C_{org}$ record, pollen distributions, nannofossils, intervals of calcification crises, and geographic location of the Italcementi section from Zaffani et al., (2018). The interval E4 was interpreted to represent the initial CIE and peak 5 was interpreted to be the beginning of the main CIE. For paleogeography of the Lombardy Basin, see Zaffani et al., (2018).

Palynological records from the Zu 3 Member contain high percentages of organic matter and organic debris derived from the terrestrial realm. Since the depositional environment is considered to have been well-oxygenated, high sedimentation rates are suggested to account for preservation of organic matter. Evidence of xerophytic elements (i.e., material from plants adapted to withstand dry environments) progressively increases throughout all Zu members, with greatest abundance in the Zu 3 Member suggesting a shift towards warmer and dryer climate in this interval (Galli et al., 2007; Jadoul et al., 2007, 2004, 1994).

Palynofacies of the Zu 3b Member contain a high percentage of diverse sporomorphs that are often associated with terrestrial phytoclasts such as cuticles, tracheids, and wood remains whereas palynofacies of the Zu 3c Member contain more marine organic matter such as foraminiferal linings, dinoflagellate cysts, and algal spores that are interpreted to reflect shallow water and normal marine conditions with high productivity and lower rates of terrestrial input (Galli et al., 2007; Jadoul et al., 2007). The Zu 3b marls also contains the pelecypod *Rhaetavicula contorta* with a latest Norian to earliest Hettangian range (McRoberts, 2008; Zaffani et al., 2018). The top of the Zu 3c Member hosts a rich fossil assemblage comprised of corals, gastropods, bivalves (large megalofontids), crinoids, benthic foraminifers (dominated by *Triasina hantkeni*), calcisponges, bryozoans, calcispongia patch-reefs,

dasycladacean algae, and coprolites, as well as the preservation of microbially-mediated oncoids, all of which disappear at the top of the Member (Galli et al., 2007; Jadoul et al., 2007; Lakew, 1990). The Rhaetian conodont *Misikella posthernsteni* was found in the Zu 3b submember (Du et al., 2020), while *Misikella ultima* was collected from the uppermost layer of the Zu 3c submember just below the Malanotte Formation (Rigo et al., 2009). This disappearance precedes palynological assemblage change at the base of the overlying Malanotte Formation and occurs within the NT2b nannofossil zone that contains characteristically late Triassic taxa including *Hayococcus floralis, Tetralithus* cassianus and *Tetralithus pseudotrifidus* (Bottini et al., 2016; Zaffani et al., 2018).

The overlying Malanotte Formation that records a transgressive event lacks the cyclicity apparent in the Zu members and consists of bioturbated mudstones-wackestones with rare thin-shelled bivalves and crinoids in the lower portion and bioclastic wackestones-packstones containing thin-shelled bivalves, ostracods, crinoids, and gastropods with some bioturbation at the top of the Formation (Galli et al., 2007; Zaffani et al., 2018 and refs therein). After a barren interval, the scarce occurrence of *Schizospharella sp.* and *Conusphaera sp.* and very rare occurrences of *Crucirhabdus minutes* indicate a switch to a Hettangian age NJT1 nannofossil zone (Bottini et al., 2016). Based on the disappearance of micro and macrofaunal taxa at the top of the Zu 3c Member and emergence of taxa in the Malanotte Formation in addition to palynological compositions, the base of the Malanotte Formation is the proposed Triassic-Jurassic boundary in the Lombardy Basin (Galli et al., 2007).

Carbon isotope excursions (CIEs) in the bulk organic carbon isotope ($\delta^{13}C_{org}$) record are a common feature of the ETE and are typically regarded to represent CAMP-induced carbon cycle perturbations through the dissociation of methane clathrates (Hesselbo et al., 2002) and/or CAMP intrusions into organic-rich and ^{13}C-depleted deposits (Davies et al., 2017), although some ETE UK studies suggest local factors are important in driving isotopic excursions (Beith et al., 2021; Fox et al., 2022b, 2020). ETE CIEs are typically used in chemostratigraphic correlations and whilst there are differing terminologies for these correlations three isotopic excursions, termed the precursor CIE, the initial CIE, and the main CIE, are often used to correlate between globally dispersed sections (e.g., Du et al., 2020; Fujisaki et al., 2018; Lindström et al., 2017). These CIEs are also recognized in the Italcementi section. However, two possible chemostratigraphic correlations are considered for the Lombardy basin, the first utilizing the $\delta^{13}C_{org}$ record from the upper Zu 3b, Zu 3c members and the Malonette Formation and second utilizing the $\delta^{13}C_{org}$ record from all Zu members and the

Malanotte Formation (Zaffani et al., 2018). Note that we use the latter of these correlations, option 2 from Zaffani et al., (2018), in which the initial CIE is placed within the Zu 3b sub-member and the main CIE is placed within the Zu 3c submember (Fig. 2).

3: Methods

All glassware was annealed at 550 °C and all apparatus was cleaned using 9:1 dichloromethane:methanol (DCM:MeOH). The surface edges of samples, collected from outcrops, were removed and samples were washed three times for 15 minutes in 9:1 DCM: MeOH to remove contamination. Samples were powdered using a SRM C+PB rock grinder and ~30 g of sample was extracted using a Milestone Start-E microwave extraction system (50 mL 9:1 DCM:MeOH) using a temperature program of 21 to 80 °C over 10 minutes and held at 80 °C for 15 minutes. Activated copper turnings (sonicated in 3M hydrochloric acid for 30 min then neutralised using Milli-Q water and solvent washed (9:1 DCM:MeOH sonicated for 15 minutes 3 times) were added to extracts to remove elemental sulfur. Samples were fractionated into saturate (4 mL *n*-hexane), aromatic (4 mL 9:1 *n*-hexane:DCM) and polar (4 mL 9:1 DCM:MeOH) fractions using activated silica gel (160 °C overnight) in annealed 4 cm Pasteur pipettes (7.5 g silica gel). Deuterated phenanthrene (d10 phenanthrene) was added as an internal standard.

The saturate fractions were analysed using an Agilent 6890 gas chromatograph (GC) fitted with a splitless injector and Agilent DB-1MS capillary column (60 m length, 0.25 mm diameter, 0.25 µm film thickness) connected to an Agilent 5973 mass spectrometer (MS). The aromatic fractions of samples were analysed using an Agilent 6890 GC fitted with a splitless injector and a DB-5MS capillary column (60 m length, 0.25 mm diameter, 0.25 µm film thickness) connected to an Agilent 2979 MS. The temperature program for the GC for both fractions was 3 °C/min from 40 °C to 325 °C where temperature was held for 30 minutes. Helium was used as the carrier gas (constant flow rate of 1.1 mL/min). Compounds were identified by comparing retention times, elution patterns, and standards (Neochema PAH mix) and PAHs reported in the literature (e.g., Grice et al., 2007, 2005; Holman et al., 2014). Bulk organic carbon isotopes ($\delta^{13}C_{org}$) and total organic carbon (TOC) values were generated by Zaffani et al., (2018).

4: Results

Abundances of LMW and HMW PAHs and their alkylated homologues and various PAH ratios were measured throughout the latest Rhaetian in the Lombardy Basin to investigate terrestrial ecological stressors during the ETE (Figures 3-5). We normalized PAHs against both grams (g) of sediment extracted and g total organic carbon (TOC) and found similar profiles between individual PAHs, and that in general most PAHs follow similar trends across each submember (supplemental information Figs S1-S4). We provide profiles of each PAH used in this study normalized to both g sediment extracted and g TOC in the supplemental information, but report PAHs normalized to g TOC in this study, except where otherwise stated. PAH compound structures and abbreviations are given in Table 1, and PAH ratios used in this study are given in Table 2.

4.1: Soil Erosion PAHs

Dibenzothiophene (DBT; S containing), dibenzofuran (DBF; O containing), and biphenyl are commonly used to infer episodes of soil erosion (Kaiho et al., 2016, 2013; Sephton et al., 2005; Wang and Visscher, 2007). These compounds follow similar profiles to each other throughout the Zu 3b and Zu 3c submembers (Fig. 3). Throughout the Zu 3b submember these PAHs remain close to 0 µg/g TOC, with the exception of very minor increases in abundance during the initial CIE (highlighted in yellow in Figs. 3-5) and toward the top of the submember during the transient and short-lived negative $\delta^{13}C_{org}$ anomaly thought to mark the beginning of the main CIE (highlighted in purple in Figs. 3-5), although values do not exceed 5 µg/g TOC. In the overlying Zu 3c submember these PAHs increase at two intervals (highlighted in pink in Figs. 3-5). The first increase to values of 99, 123, and 138 µg/g TOC for DBT, DBF, and biphenyl, respectively, occurs stratigraphically lower in the submember (Sample Zu17) and is short-lived. The second and largest increase occurs stratigraphically higher and exhibits a more prolonged increasing then decreasing pattern with maximum values of 99, 172 and 269 µg/g TOC extracted for DBT, DBF, and biphenyl, respectively (Samples Zu25-13, Zu21-13, Zu13, Zu12, Zu15b-13).

4.2: Combustion-derived PAHs

PAHs containing between three and seven rings commonly used as wildfire indicators in the geological record include phenanthrene, fluoranthene, pyrene, benzo[*a*]anthracene, chrysene and triphenylene, benzo[*bjk*]fluoranthene, benzo[*e*]pyrene, benzo[*a*]pyrene, indeno[1,2,3-cd]pyrene, benzo[*ghi*]perylene, and coronene (e.g., Nabbefeld et al., 2010) (Table 1). However, despite frequently being attributed to paleowildfire events such compounds can have a petrogenic (i.e., oil/coal-derived) origin as well as a pyrogenic (i.e., fire-derived) origin, and are therefore not exclusively derived from combustion (Stogiannidis and Laane, 2015; Yunker et al., 2002). Hence, we term these compounds as potentially combustion-derived PAHs (PAH_{PCD}). Since these compounds follow similar trends to one another whether normalized to TOC or g of sediment extracted (supplementary material), we combine the concentrations of these PAHs ($\sum PAH_{PCD}$) to serve as a first order paleowildfire indicator in the sedimentary record. Further scrutiny of this record in terms of wildfire intensity, smoke signal versus char/burn residue, burn material, and pyrogenic versus petrogenic sources is described in detail below. In the Zu 3b submember, $\sum PAH_{PCD}$ abundances generally remain low, reaching maximum values of 1.3mg/g TOC. However, when the $\sum PAH_{PCD}$ record is normalized to g of sediment extracted, two short-lived increases occur, once at the onset of the initial CIE and again toward the top of the submember during the transient and short-lived negative $\delta^{13}C_{org}$ anomaly regarded as the onset of the main CIE (Fig. 3). Notably, these increases coincide with increases in TOC and only marginally increase when normalized against TOC, and therefore likely represent increased organic matter input/preservation. $\sum PAH_{PCD}$ abundances in the overlying Zu 3c submember are much greater than those of the Zu 3b submember and show profiles analogous to that of DBT, DBF, and biphenyl i.e., a short-lived increase reaching values of 7.3 mg/g TOC followed by a prolonged increase-decrease profile where maximum values reach 12.2 mg/g TOC (Fig. 3). All PAHs investigated in this study reach their maximum value within the Zu 3c submember, with LMW PAH_{PCD} mostly having greater concentrations than HMW (except for chrysene and triphenylene and benzo[*e*]pyrene; see supplementary information). Interestingly, the abundances of five, six and seven-ringed PAH_{PCD} in the Zu 3b submember have comparable concentrations with those in the Zu 3c submember, whereas abundances of three and four-ringed PAH_{PCD} in the Zu 3b submember are much lower than those of the Zu 3c submember (Fig. 3; Supplemental Information). To investigate this further we consider the ratio of PAHs to determine burn intensity, smoke vs. burn/char residue input, and pyrogenic or petrogenic origins for PAH_{PCD} .

4.3: PAH ratios for burn intensity and smoke or char/burn residue

The abundance of HMW compared to LWM PAH_{PCD} is interpreted to represent the intensity of wildfire burning, due to more higher temperature fire events producing greater quantities of PAHs with higher ring numbers (e.g., Finkelstein et al., 2005; Kaiho et al., 2020). Here, we compare the abundance of five-ringed PAH_{PCD} (benzo[*bjk*]fluoranthene, benzo[*a*]pyrene, and benzo[*e*]pyrene) to phenanthrene (5/3-ringed PAH_{PCD}), and six and seven-ringed PAH_{PCD} (benzo[*ghi*]perylene, indeno[1, 2, 3-cd]pyrene, and coronene) to phenanthrene (6 & 7/3-ringed PAH_{PCD}; see Table 2), to indicate burn intensity. Additionally, a similar ratio of PAH_{PCD} is used to infer smoke vs. char/burn residue input (Table 2) since smoke, that can travel great distances from the burn source (up to ~10,000 km), contains greater abundances of phenanthrene, fluoranthene, and pyrene whereas char/burn residue, that is typically deposited closer to the source and travels relatively shorter distances (up to ~10 km), contains relatively more benzo[*a*]anthracene, chrysene and triphenylene, benzo[*bjk*]fluoranthene, benzo[*e*]pyrene, benzo[*a*]pyrene, indeno[1,2,3-cd]pyrene, and benzo[*ghi*]perylene (Karp et al., 2020 and refs therein). Based on Karp et al., (2020), values of the ratio of these compounds (Table 2) greater than ~0.75-0.8 imply predominant smoke input whereas values below ~0.75-0.8 imply predominant char/burn residue input. Given the similarities between these ratios, but different interpretations, we consider the following: High abundances of five, six, and seven-ringed PAH_{PCD} and increases in 5/3-ringed PAH_{PCD} and 6 & 7/3-ringed PAH_{PCD} ratios that drive a predominant char/burn residue input could reflect higher intensity burn events closer to the site of deposition, although secondary transport of HMW PAH_{PCD} should also be considered. Contrastingly, when abundances of five, six, and seven-ringed PAH_{PCD} and ratios of 5/3-ringed PAH_{PCD} and 6 & 7/3-ringed PAH_{PCD} are low, and phenanthrene abundances (in addition to other four-ringed PAH_{PCD}) are high supporting a predominant smoke input, PAH_{PCD} could reflect smoke signals and/or less intense wildfire closer to the deposition site.

We also consider changes in these ratios, and the abundances of DBT, DBF, biphenyl, and $\sum PAH_{PCD}$, with changes in the ratio of *n*-alkanes to determine the input of terrestrial material. Short chain $C_{15\text{-}21}$ *n*-alkane biomarkers (molecular fossils) typically originate from algae and photosynthetic bacteria (Cranwell et al., 1987) whereas long chain odd-numbered *n*-alkanes originate from land plant leaf waxes (Eglinton et al., 1962). Thus, ratios of terrestrial-derived odd-numbered $C_{27\text{-}35}$ *n*-alkanes (*n*-$C_{27\text{-}35}$) to the sum of odd-numbered *n*-$C_{27\text{-}35}$ and marine-derived *n*-$C_{17\text{-}21}$ greater than 0.5 are used to reflect a greater input of terrestrial material (e.g., Boudinot and Sepúlveda, 2020). Values of this ratio are variable throughout the section

(Fig. 3), but generally show greater terrestrial input in the Zu 3b submember and greater marine input in the Zu 3c, consistent with the changes of organic matter type between submembers described in section 2.

Table. 1: PAH compounds used in this study and their structure.

Compound	Abbreviation	Molecular Weight	Structure	
Biphenyl	B	154		LMW
Dibenzofuran	DBF	168		
Phenanthrene	P	178		
Dibenzothiophene	DBT	184		
Fluoranthene	Fl	202		
Pyrene	Py	202		
Benzo[*a*]anthracene	BaA	228		
Chrysene	C*	228		
Triphenylene	T*	228		
Benzo[*e*]pyrene	BeP	252		HMW
Benzo[*a*]pyrene	BaP	252		
Benzo[*bjk*]fluoranthene	BbjkF	252		
Indeno[1,2,3-cd]pyrene	IP	276		
Benzo[*ghi*]perylene	BghiP	276		
Coronene	COR	300		

*Chrysene and triphenylene are shown in this table as two separate compounds, but co-elute in the GC-MS profile, and are thus given the abbreviation C&T in text. Compounds are given in order of molecular weight.

368 Table 2: PAHs and their application in this study.

PAH	Compounds/Equation and Interpretation		References
Potentially combustion-derived PAH compounds (PAH_{PCD})	Phenanthrene (P), fluoranthene (Fl), pyrene (Py), benzo[a]anthracene (BaA), chrysene and triphenylene (C&T), benzo[bjk]fluoranthene (BbjkF), benzo[e]pyrene (BeP), benzo[a]pyrene (BaP), indeno[1,2,3-cd]pyrene (IP), benzo[ghi]perylene (BghiP), and coronene (COR)		Various PAH studies (e.g., Nabbefeld et al., 2010)
5/3-**ringed PAH_{PCD}**	$\frac{\text{benzo}[bjk]\text{fluoranthene} + \text{benzo}[a]\text{pyrene} + \text{benzo}[e]\text{pyrene}}{\text{phenanthrene}}$	Increase with higher temperature burning events	Based on evidence that increasing burn intensity produces relatively more HMW PAH (e.g., Finkelstein et al., 2005; Kaiho et al., 2020)
6 & 7/3-**ringed PAH_{PCD}**	$\frac{\text{benzo}[ghi]\text{perylene} + \text{indeno}[1,2,3-\text{cd}]\text{pyrene} + \text{coronene}}{\text{phenanthrene}}$	Increase with comparatively higher temperature burning events than five/three-ringed PAH_{PCD}	
Ratio of selected dimethylphenanthrene isomers (**DMPx**)	$\frac{1,7 + 2,6\|3,5\ \text{DMP}}{1,2 + \ 1,7 + 2,6\|3,5\ \text{DMP}}$	0.2 – 0.6 = angiosperms 0.6 – 0.9 = grasses > 0.9 = conifers	Kappenberg et al., (2019)
Alkylated PAH derivative Index (APDI)	$f''(x) - f'(2)$ = APDI Where $f''(x) = 2a$ and $f'(x) = 2a + b$ Using $f(x) = ax^2 + bx + c$	Negative values = petrogenic or conifer combustion Positive values = pyrogenic	Karp et al., (2020)
Source of PAH_{PCD}	$\frac{\text{methylphenanthrene}}{\text{phenanthrene}}$	> 1 = petrogenic < 1 = pyrogenic	(Stogiannidis and Laane, 2015; Yunker et al., 2002)
	$\frac{1,7\ \text{DMP}}{1,7 + 2,6\ \text{DMP}}$	> 0.7 pyrogenic 0.45 – 0.7 = mixed source	
	$\frac{\text{indeno}[1,2,3-\text{cd}]\text{pyrene}}{\text{indeno}[1,2,3-\text{cd}]\text{pyrene} + \text{benzo}[ghi]\text{perylene}}$	> 0.2 = pyrogenic < 0.2 = petrogenic	
	$\frac{\text{benzo}[a]\text{anthracene}}{\text{benzo}[a]\text{anthracene} + \text{chrysene and triphenylene}}$	> 0.35 = pyrogenic 0.2 – 0.35 = mixed source < 0.2 = petrogenic	
	$\frac{\text{fluoranthene}}{\text{pyrene} + \text{fluoranthene}}$	> 0.5 = pyrogenic/primary < 0.5 = petrogenic/degraded	
Smoke vs. char/burn residue	$\frac{\text{phenanthrene} + \text{Fluoranthene} + \text{pyrene}}{\text{phenanthrene} + \text{Fluoranthene} + \text{pyrene} + \text{Benzo}[a]\text{anthracene} + \text{chrysene} + \text{triphenylene} + \text{Benzo}[bjk]\text{fluoranthene} + \text{benzo}[e]\text{pyrene} + \text{benzo}[a]\text{pyrene} + \text{indeno}[1,2,3-\text{cd}]\text{pyrene} + \text{benzo}[ghi]\text{perylene}}$	> ~0.75-0.8 = smoke < ~0.75-0.8 = burn/char residue	Karp et al., (2020)

369

370

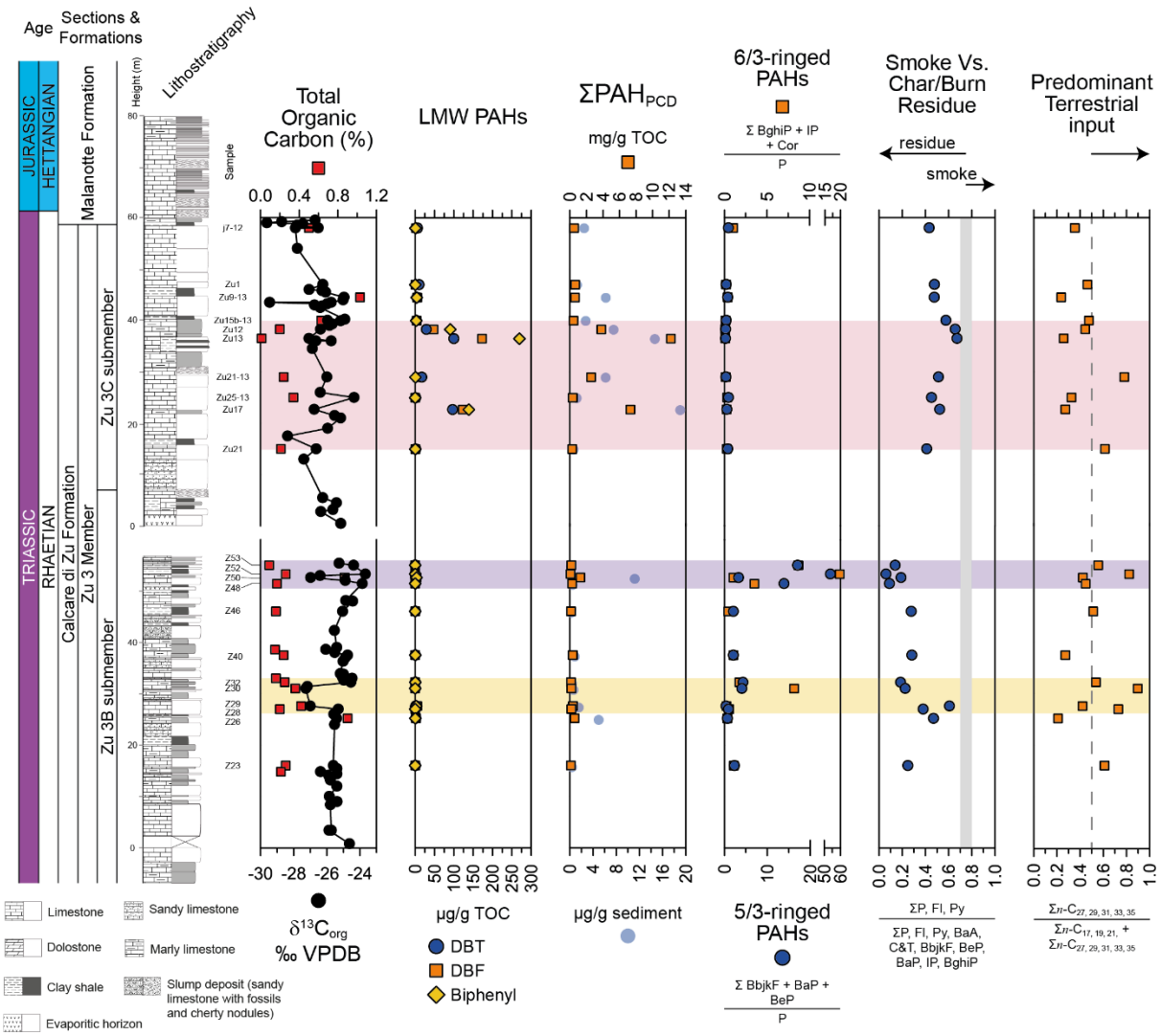

371

372

373 Figure 3: PAHs and *n*-alkane ratios in relation to the $\delta^{13}C_{org}$ and total organic carbon (TOC) record at the
374 Italcementi section in the Lombardy Basin. Note that the $\sum PAH_{PCD}$ is the sum of phenanthrene (P), fluoranthene
375 (Fl), pyrene (Py), benzo[*a*]anthracene (BaA), chrysene and triphenylene (C&T), benzo[*bjk*]fluoranthene (BbjkF),
376 benzo[*e*]pyrene (BeP), benzo[*a*]pyrene (BaP), indeno[1,2,3-cd]pyrene (IP), benzo[*ghi*]perylene (BghiP), and
377 coronene (COR). For full compound structures and abbreviations see Table 1 and for PAH ratios see Table 2.
378 Ratios of *n*-alkanes ($\sum n\text{-}C_{27,29,31,33,35}/(\sum n\text{-}C_{17,19,21,27,29,31,33,35}$) greater than 0.5 are used to indicate greater input of
379 terrestrial material. Yellow interval (lower) indicates the initial CIE, purple interval (middle) highlights the upper
380 Zu 3b increases in PAH ratios to determine increased burn intensity and lowest values in the smoke vs. char/burn
381 residue, and the pink interval (top) highlights the Zu 3c pulsed and prolonged increases in LMW PAHs and
382 $\sum PAH_{PCD}$ described in the results. These highlighted intervals are used throughout Figures 3-5. Lithostratigraphy
383 from Zaffani et al., (2018).

384

Throughout the Zu 3b submember, two increases in the 5/3-ringed PAH_{PCD} and 6 & 7/3-ringed PAH_{PCD} ratios are observed (Fig. 3). Firstly, within the upper portion of the initial CIE the 6 & 7/3-ringed PAH_{PCD} ratio show increases coincident with minor shifts in the smoke versus char/burn residue ratio towards more negative values and increases in terrestrial input. However, these changes do not coincide with any changes in the $\sum PAH_{PCD}$ record. Secondly, in the upper Zu 3b submember, between 51 and 55 m, the 5/3-ringed PAH_{PCD} and 6 & 7/3-ringed PAH_{PCD} ratios increase above the typical background levels observed throughout the Zu 3b and 3c submembers. The largest values of both these ratios coincide with increases in terrestrial input and the lowest values in the smoke vs. char/burn residue ratio throughout the section, suggesting a more intensive burn event and/or a prominent char/burn residue input. Increases in the 5/3-ringed PAH_{PCD} and 6 & 7/3-ringed PAH_{PCD} ratios superficially appear coincident with most negative values in the upper Zu 3b $\delta^{13}C_{org}$ anomaly marking the onset of the main CIE and minor increases in $\sum PAH_{PCD}$. However, increases in these ratios occur at the termination of the $\delta^{13}C_{org}$ anomaly. In fact, the most negative values in the $\delta^{13}C_{org}$ anomaly at this interval (52.6 m) coincide with minor increases in $\sum PAH_{PCD}$ and the lowest values in the ratios of 5/3-ringed PAH_{PCD} and 6 & 7/3-ringed PAH_{PCD}. Regardless, this cluster between 51 and 55 m in the Zu 3b submember (samples Z48, Z50, Z52, and Z52 in Fig. 3; 4) shows the most consistent increases in HMW PAH_{PCD} compared to LMW PAH_{PCD} and is typically dominated by chrysene and triphenylene, benzo[*ghi*]perylene, benzo[*e*]pyrene, and to a lesser extent coronene (supplementary information) with the best evidence of predominant char/burn residue input (Fig. 3). Above in the Zu 3c submember, 5/3 and 6 & 7/3-ringed PAH_{PCD} ratios are very low, and the smoke versus char/burn residue signal shows the highest values, driven by increases in phenanthrene, indicating a more predominant smoke input throughout the Zu 3c submember.

4.4: PAH ratios for pyrogenic versus petrogenic source

Various PAH ratios are employed to determine whether PAHs often attributed to paleowildfire events have a pyrogenic (i.e., fire-derived) or a petrogenic (i.e., oil/coal-derived) origin. Such ratios were successfully employed during the ETE (Fox et al., 2022b; Song et al., 2020) and more recent grassland expansion events (Karp et al., 2018). In this study, we employ five ratios to discern whether PAH_{PCD} have a petrogenic or pyrogenic origin (Table 2). These include indeno[1,2,3-cd]pyrene/indeno[1,2,3-cd]pyrene + benzo[*ghi*]perylene (IP/IP+BghiP),

benzo[*a*]anthracene/benzo[*a*]anthracene + chrysene and triphenylene (BaP/BaP+C&T), and 1,7 dimethylphenanthrene/1,7 + 2,6 dimethylphenanthrene (1,7/1,7+2,6 DMP) based on modern PAH abundances (Stogiannidis and Laane, 2015; Yunker et al., 2002) and ratios of methylphenanthrene/phenanthrene (MP/P) and fluoranthene/fluoranthene + pyrene (Fl/Fl+Py) successfully applied in previous mass extinction and grassland ecology studies (Karp et al., 2018; Song et al., 2020).

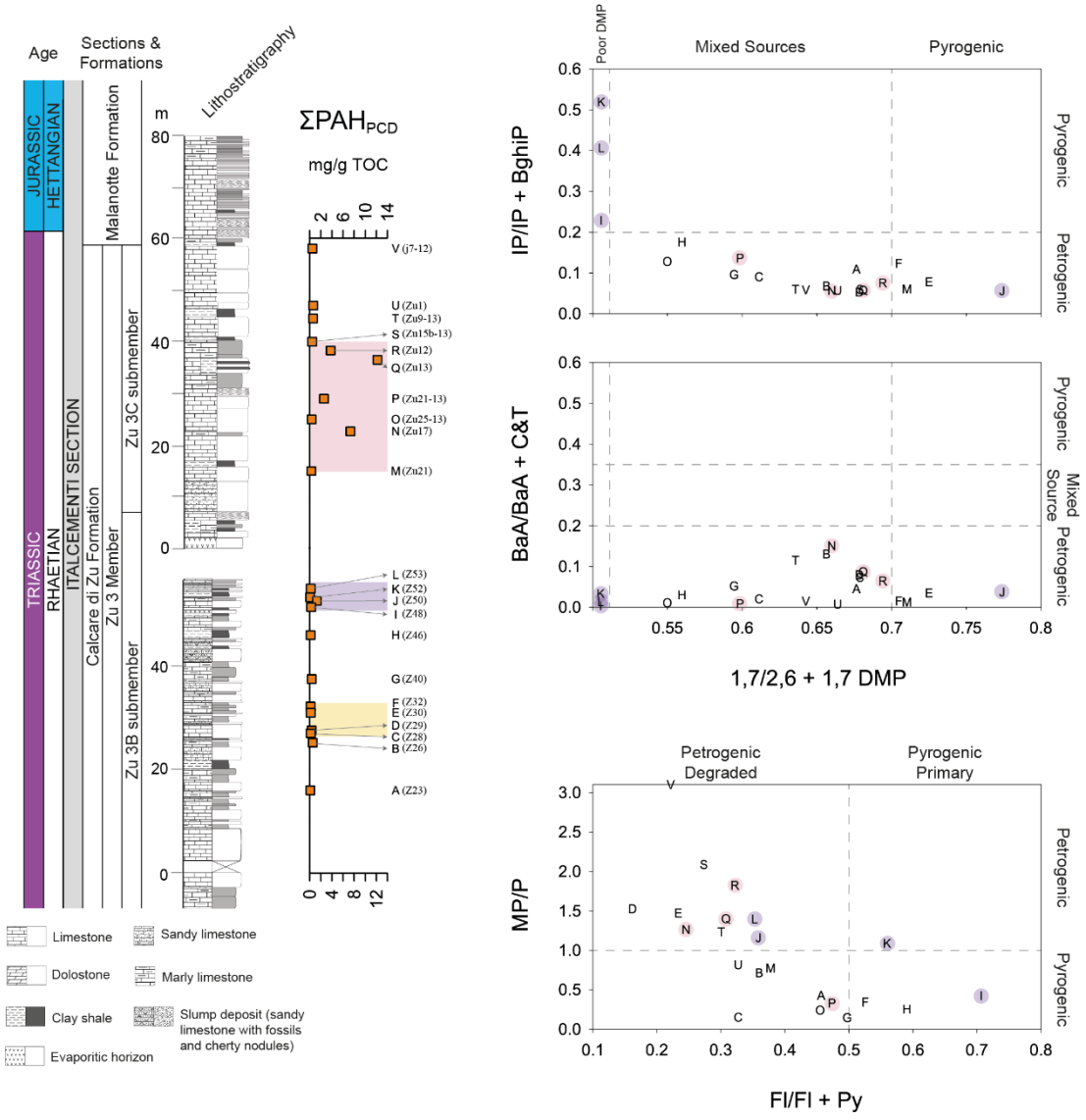

Figure 4: Ratios of PAHs to better determine the origin of PAHs relative to the $\sum PAH_{PCD}$ records. Samples are assigned a corresponding letter (A to V) for clearer visualisation of ratios. Highlighted areas behind letters in PAH ratios correspond to highlighted intervals in $\delta^{13}C_{org}$ and $\sum PAH_{PCD}$ plot. Note that samples Z48 (I), Z52 (K), and Z53 (L) have poor dimethylphenanthrene (DMP) chromatograms and ratios of 1,7/1,7 + 2,6 DMP could not be calculated.

All samples plot within the petrogenic region when considering the ratio of BaP/BaP+C&T and all but three samples (Z48, Z52, Z53) plots within the petrogenic region when considering the ratio of IP/IP+BghiP (Fig. 4). Notably it is these three samples that show increased ratios of 5/3-ringed PAH_{PCD} and 6 & 7/3-ringed PAH_{PCD}. Four samples plot within the pyrogenic region (Z30, Z32, Z50, and Zu21) and all others in the mixed sources region when considering the ratio of 1,7/1,7+2,6 DMP (note that samples Z48, Z52, Z53 produced very low quantities of DMP that were unable to produce this ratio). Using the MP/P ratio approximately half of the samples plot as pyrogenic (Fig. 4) and those intervals that contain elevated $\sum PAH_{PCD}$ concentrations and increases in the ratios of 5/3-ringed PAH_{PCD} and 6 & 7/3-ringed PAH_{PCD} typically plot within the petrogenic region. Importantly, for this ratio, abundances of phenanthrene and methylphenanthrene can be affected by biodegradation and maturity (Bennett and Larter, 2008; Cassani et al., 1988), however, we find neither of these diagenetic effects in these samples (see supplemental information). The ratio of Fl/Fl+Py is used both as an indicator of pyrogenic *versus* petrogenic input (Song et al., 2020; Yunker et al., 2002) and to determine whether PAHs represent a degraded or primary signal (Arias et al., 2017; Karp et al., 2018 and refs therein). All but four samples (Z32, Z46, Z48, and Z52) plot within the degraded/petrogenic region.

An additional proxy for determining pyrogenic vs. petrogenic origins is the profiles of phenanthrene and its alkylated homologues (Karp et al., 2020). In previous burn experiments, gymnosperms and angiosperms show a "staircase" pattern of phenanthrene and its methylated homologues, that is phenanthrene having the greatest abundance, methylphenanthrene having the second greatest abundance, dimethylphenanthrene having the third greatest abundance, and trimethylphenanthrene having the fourth greatest abundance (e.g., see sample Z23 in Fig. S8). However, conifer burning produces a pattern that differ from the typical "staircase" pattern and show greatest abundances of methylphenanthrene and/or dimethylphenanthrene (Karp et al., 2020). To quantify this, Karp et al., (2020) generated the Alkylated PAH Derivative Index (APDI) that fits a parabolic curve to a normalized alkylated PAH distribution. For phenanthrene and its alkylated derivatives, when values in the APDI are positive (i.e., concave upward parabolic curve and therefore more phenanthrene compared to its alkylated derivatives) PAH_{PCD} represent a pyrogenic source. However, when APDI values are negative (i.e., concave downward parabolic curve and therefore more alkylated phenanthrene derivatives compared to phenanthrene) they represent a petrogenic or conifer combustion source since conifers typically produce patterns of phenanthrene and its methylated homologues that deviate from the

463 "staircase" pattern. In this study, APDI values are generally sporadic in the Zu3b submember,
464 particularly in the initial CIE (Fig. 5). During the $\delta^{13}C_{org}$ anomaly thought to mark the onset of
465 the main CIE values are negative (between -5.1 and -20.9) with the exception of one sample
466 (Z48) at the onset of the $\delta^{13}C_{org}$ anomaly that shows positive values (54.6). Above, in the Zu3c
467 submember, during the first increase in $\sum PAH_{PCD}$ APDI values are marginally negative (-6.2)
468 whereas in the second and more prolonged $\sum PAH_{PCD}$ increase APDI values are both positive
469 and negative; $\sum PAH_{PCD}$ and APDI values for sample Zu21-13 are 2.6 mg/g TOC and 45.0,
470 respectively, for sample Zu13 12.2 mg/g TOC and -11, respectively, and for sample Zu12 3.8
471 mg/g TOC and -20.0, respectively. Based on APDI scores, and corroborated visually
472 (supplemental information Fig. S8) , samples with increased $\sum PAH_{PCD}$ abundances most-often
473 deviate from the "staircase" alkylation pattern (Fig. 5).

474

475 **4.5: PAHs and PAH ratios for source of burn material**

476 Finally, to help determine the material burned we investigated concentrations of retene
477 and ratios of dimethylphenanthrene (DMP). Retene is evidenced to derive from conifer
478 combustion (Ramdahl, 1983) and is typically used in the geological record to indicate such
479 conifer combustion. However, other sources for retene such as phytoplankton and bryophytes
480 are also recognized (Romero-Sarmiento et al., 2010; Wen et al., 2000) and other evidence
481 supports retene may not be unique to conifer combustion, with coal combustion also playing
482 an important role for increases in retene concentrations (Shen et al., 2012). In chromatograms
483 of our samples, retene peaks are typically very low, and do not exceed peaks of
484 trimethylphenanthrene, except for samples Zu21-13 and Zu25-13 that show more elevated
485 peaks (see supplemental information Fig. S10). However, when quantified, concentrations of
486 retene tend the follow trends of $\sum PAH_{PCD}$; concentrations remain low throughout the Zu3b
487 submember, reaching maximum concentrations of 0.9 µg/g TOC and in the succeeding Zu3c
488 submember concentrations show an abrupt increase to a value of 10.4 µg/g TOC then a more
489 prolonged increase to maximum values of 17.5 µg/g TOC.

490 Kappenberg et al., (2019), in addition to showing ratios of IP/IP+BghiP greater than
491 0.34 and Fl/Fl+Py greater than 0.4 are indicative of pyrogenic input, found that conifer
492 combustion is dominated by 1,7-dimethylphenanthrene, whereas angiosperm combustion is
493 dominated by 1,2-DMP. Thus, the ratio of (1,7 + 2,6|3,5)/(1,2 + 1,7 + 2,6|3,5) DMP isomers
494 (DMPx) can be used to indicate angiosperms when values fall between 0.2 and 0.6 and

gymnosperms when >0.9 (Kappenberg et al., 2019). Although conifers dominated Mesozoic flora, particularly in the Triassic and Jurassic, and the replacement and expansion of angiosperms in Europe did not occur until the Cretaceous (Coiffard et al., 2012), we investigate DMPx values to observe changes in this ratio in deeper time and to help serve as evidence of conifer combustion in addition to retene concentrations. DMPx values throughout the section vary between 0.77 and 0.94 supporting conifer combustion.

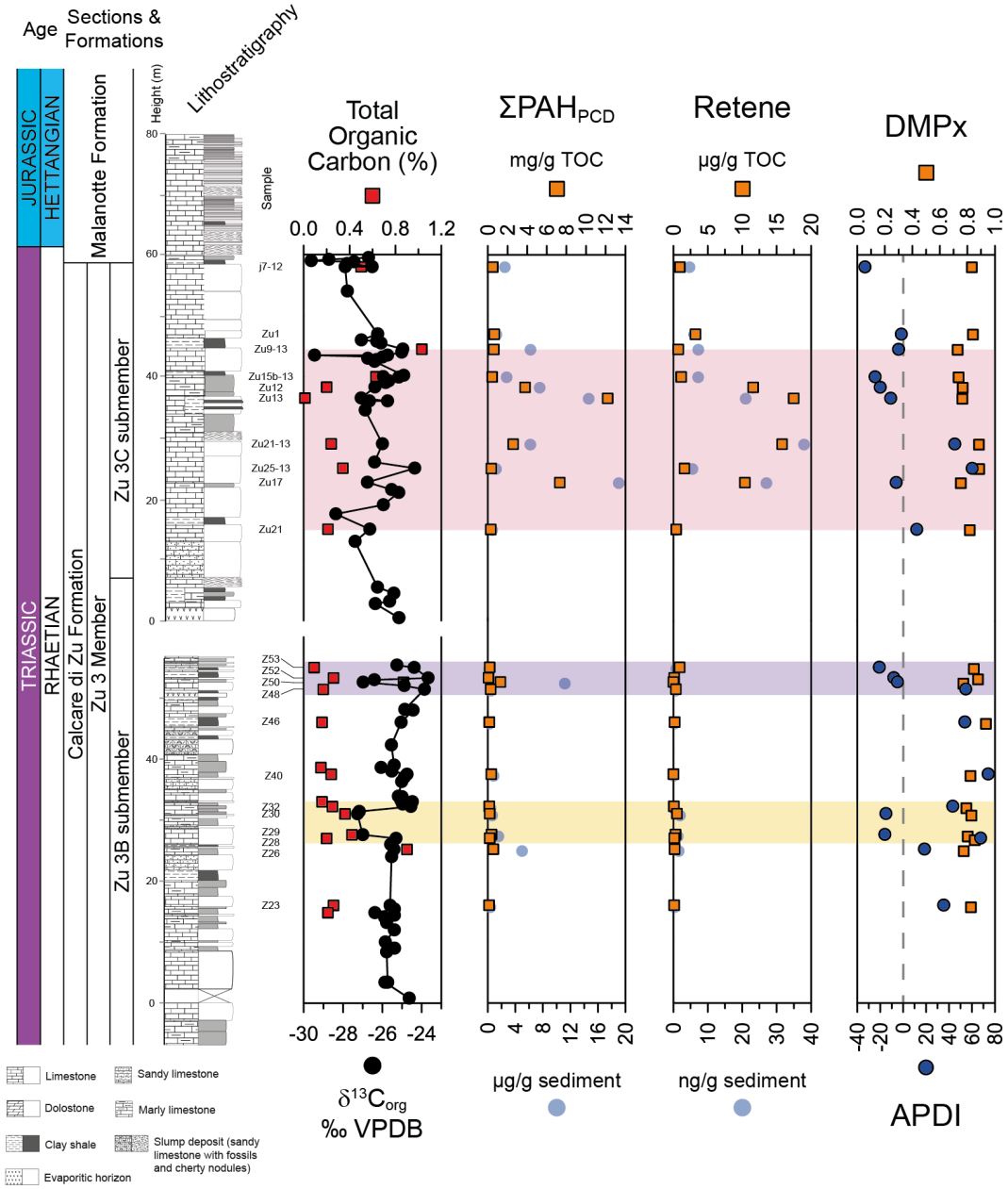

Figure 5: Abundances of retene, the APDI, and the DMPx ratio compared to records of $\sum PAH_{PCD}$, $\delta^{13}C_{org}$, and total organic carbon. Note that the dashed line in the ADPI plot at 0 helps indicate which samples are pyrogenic (above 0 and right of the dashed line) and petrogenic or conifer burn material (below 0 and left of the dashed line).

5: Discussion

5.1: Fire events in Northern Italy during the ETE

Based on various PAH ratios, the samples of the Italcementi section mostly show a mixed pyrogenic and petrogenic source, although those samples which show the best evidence of a pyrogenic origin (i.e., those that plot within the pyrogenic and pyrogenic/primary window) are related to the initial CIE and the negative $\delta^{13}C_{org}$ anomaly above (Fig. 4). Of these two intervals, only the upper Zu 3b negative $\delta^{13}C_{org}$ anomaly shows increases in $\sum PAH_{PCD}$, *albeit* minor, that occur alongside a char/burn residue-dominated signal supporting fire in close proximity to the depositional site and increases in HMW PAHs attributed to more intense wildfire burning (e.g., Finkelstein et al., 2005; Kaiho et al., 2020). We interpret this event to represent a short-lived but intense paleowildfire event close to the site of deposition that coincides with the end of a $CaCO_3$ productivity crisis and in close proximity to the onset of the nannofossil calcification crisis based on fossil occurrences and lithology (see Bottini et al., (2016) and Zaffani et al., (2018) and references therein) (Fig. 2; 3), thereby linking terrestrial and marine ecosystem perturbations similar to the newly identified extinction horizon in the SW UK (Fox et al., 2022b, 2022a; Wignall and Atkinson, 2020). Further studies on terrestrial ecosystem stresses, such as land plant mutagenesis (e.g., Lindström et al., 2019) and soil erosion (e.g., van de Schootbrugge et al., 2020) in addition to terrestrial burning events, should be considered in relation to the timing of marine environmental stressors, including redox and pH changes (e.g., Bond et al., 2022; He et al., 2022), to help determine timing offsets (if any) between the terrestrial and marine environmental stressors that resulted in extinction.

When considering APDI values, samples from the $\delta^{13}C_{org}$ anomaly in the upper Zu 3b submember and elevated $\sum PAH_{PCD}$ values in the Zu 3c submember typically have negative APDI values and therefore phenanthrene and its methylated homologues deviate from the typical "staircase" pattern suggesting a petrogenic origin. However, burning of conifer material also yields negative APDI values (Karp et al., 2020). Although distant relatives of modern angiosperms likely evolved more than 250 million years ago (Beaulieu et al., 2015) it is generally accepted that the end-Triassic was dominated by gymnosperms and ferns and Rhaetian palynological records are inundated with conifer pollen and punctuated by fern proliferation (Wignall and Atkinson, 2020 and refs therein). Thus, increases in five, six, and seven-ringed PAH_{PCD} and ratios of 5/3-ringed and 6 & 7/3-ringed PAH_{PCD} in the upper Zu 3b submember that suggest an intense burning event could represent the incomplete combustion

538 of conifer material, although no increases in retene are observed at this interval. Possibly the
539 more prolonged increases in $\sum PAH_{PCD}$ in the Zu 3c submember better represents incomplete
540 combustion of conifers given these increases coincide with increases in retene (Fig. 5). Since
541 increases in $\sum PAH_{PCD}$ in the Zu 3c submember are dominated by LMW PAH_{PCD}, and ratios of
542 5/3-ringed PAH_{PCD} and 6 & 7/3-ringed PAH_{PCD} are low, this interval could represent
543 predominant smoke input from conifer burning. This smoke input may be related to intensive
544 paleowildfire activity further from the deposition site given that smoke aerosols that contain
545 abundant LMW PAH_{PCD} can travel great distances. Song et al., (2020) suggest southward
546 displacement of the Intertropical Convergence Zone based on PAH profiles from China. Given
547 that these sections are at similar latitudes, similar processes could be at play and smoke signals
548 could originate from higher latitudes. However, Tegner et al., (2020) argue that ETE platinum
549 group element distributions and concentrations are governed by wind and atmospheric
550 circulations, in addition to preservation, and are responsible for differing concentrations
551 between sections at the global scale. These processes would also heavily impact smoke signals
552 and therefore may also affect concentrations of PAHs associated with smoke signals in the
553 sedimentary record, complicating possible fire source origins. Additionally, since
554 concentrations of HMW PAH_{PCD} also increase and reach their highest concentrations within
555 the Zu 3c submember, *albeit* lower than LMW PAH_{PCD} (with the exception of chrysene and
556 triphenylene and benzo[*e*]pyrene; see supplementary information), less intensive wildfire
557 activity cannot be entirely ruled out. Finally, other PAH ratios to determine pyrogenic *versus*
558 petrogenic input mostly plot within the petrogenic region and therefore increases in petrogenic
559 input may also be responsible for increases in PAH_{PCD} in the Zu 3c submember, and possibly
560 related to soil erosion given increases in DBT, DBF, and biphenyl (see section 5.2).

561 The large inputs of PAH_{PCD} in the Zu 3c submember may also serve as a secondary
562 ecological stress in addition to fire given the toxic nature of PAHs. The dose required to kill
563 50% of a population (lethal dosage; LD_{50}) is typically greater in LMW than HMW PAHs,
564 however, since LMW PAHs are more soluble they are typically regarded as more toxic than
565 their HMW counterparts (Peters et al., 2004). For example, phenanthrene is twice as toxic as
566 pyrene when exposed to the freshwater zooplankton *Daphnia magna* when considering the
567 solubility and LD_{50} of these compounds. (Peters et al., 2004). Therefore, the large increases in
568 phenanthrene in the Zu 3c submember (supplemental information Fig. S2) may also provide
569 ecological stress to the marine realm given the toxic nature of this PAH.

570

5.2: Soil erosion events in North Italy during the ETE

LMW PAH compounds are often overlooked in ETE organic geochemical studies despite their importance as proxies of soil erosion. Here, we consider the profiles of the LMW PAHs biphenyl, DBT, and DBF. In the Italcementi section of the Lombardy basin, increases in these compounds occur in the Zu 3c submember that contains more marine organic matter (Fig. 3; section 2). Much like previous studies from the end-Permian mass extinction, these compounds show similar profiles (Fenton et al., 2007) suggesting a common origin or source. Whilst the precise plant precursor of these compounds are not completely understood (Fenton et al., 2007), there is good evidence that DBT, DBF, and biphenyl derive mostly from terrestrial material; DBF may derive from the lignin of woody plants, lichens, and the dehydration of cellulose/polysaccharides (Kaiho et al., 2013 and refs therein), and DBT and biphenyl may also derive from the lignin of woody plants (Fenton et al., 2007 and refs therein). Thus, abundant biphenyl, DBT, and DBF are commonly used to infer episodes of soil erosion (Kaiho et al., 2016, 2013; Sephton et al., 2005; Wang and Visscher, 2007). The elevated abundances of these PAHs in the Zu 3c submember point to a source from soil erosion processes surrounding the time of the ETE, as evidenced in the Bristol Channel Basin using similar PAH distributions (Fox et al., 2022b) and across much of Europe through evidence of reworked palynomorphs (van de Schootbrugge et al., 2020). However, the coinciding increases with $\sum PAH_{PCD}$ in the Zu 3c submember, driven predominantly by phenanthrene (Fig. 3; 4) must be addressed.

In the Zu 3c submember, the sum of DBT, DBF and biphenyl correlate well with abundances of phenanthrene (r^2 = 0.9) (supplemental information Fig. S5), suggesting a common process is responsible for their elevated concentrations. Good correlation between cyclical increases in DBT, DBT and PAH_{PCD} in the Bristol Channel Basin, SW UK were regarded to represent increased abundances of terrestrial material and possibly soil-stored PAHs since PAH_{PCD} had a characteristic petrogenic signal (Fox et al., 2022b). PAH ratios in this study mostly fall within a petrogenic or mixed source window, thus similar processes may be at play. Additionally, fire events during more recent and other biotic crises are evidenced to drive input of terrestrial material (Boudinot and Sepúlveda, 2020 and refs therein). Possibly the increases in $\sum PAH_{PCD}$ could reflect low intensity fire events which account for relatively minor inputs of terrestrial material including DBT, DBF, and biphenyl. However, we find no increases in terrestrial material from *n*-alkanes coincident with increases in LMW PAHs (Fig. 3). Ratios of DBF to phenanthrene greater than 0.1 are interpreted to represent soil erosion events during the ETE and other extinction events (Kaiho et al., 2022, 2013; Philp and

DeGarmo, 2020). Although ratios of DBF/phenanthrene increase during periods of elevated DBT, DBF, and biphenyl abundances, values of DBF/phenanthrene do not exceed 0.1. Increases in DBF/phenanthrene ratios in the Zu 3c submember are consistent with a propagation to a mid to inner carbonate ramp (see section 2) as ratios from deep water sections are typically very low and those closer to terrestrial settings have comparably higher values (Kaiho et al., 2013). However, in other extinction events DBF/phenanthrene evidence of soil erosion events from Italian and Chinese sedimentary sections that represent mid to inner shelfs are typically much greater than 0.1 (Kaiho et al., 2013), i.e., values not observed in this study. Regardless of the exact mechanism, the abundances of DBT, DBF and biphenyl are much lower than abundances of PAH_{PCD} (Fig. 3; 4; supplemental information), thus fire-related events during this interval are likely a more significant terrestrial ecosystem stress compared to soil erosion at this location, although the introduction of PAH_{PCD} from petrogenic sources due to weathering/soil erosion cannot be entirely ruled out due to discrepancies in PAH source ratios and correlation between the sum of DBT, DBF and biphenyl and phenanthrene.

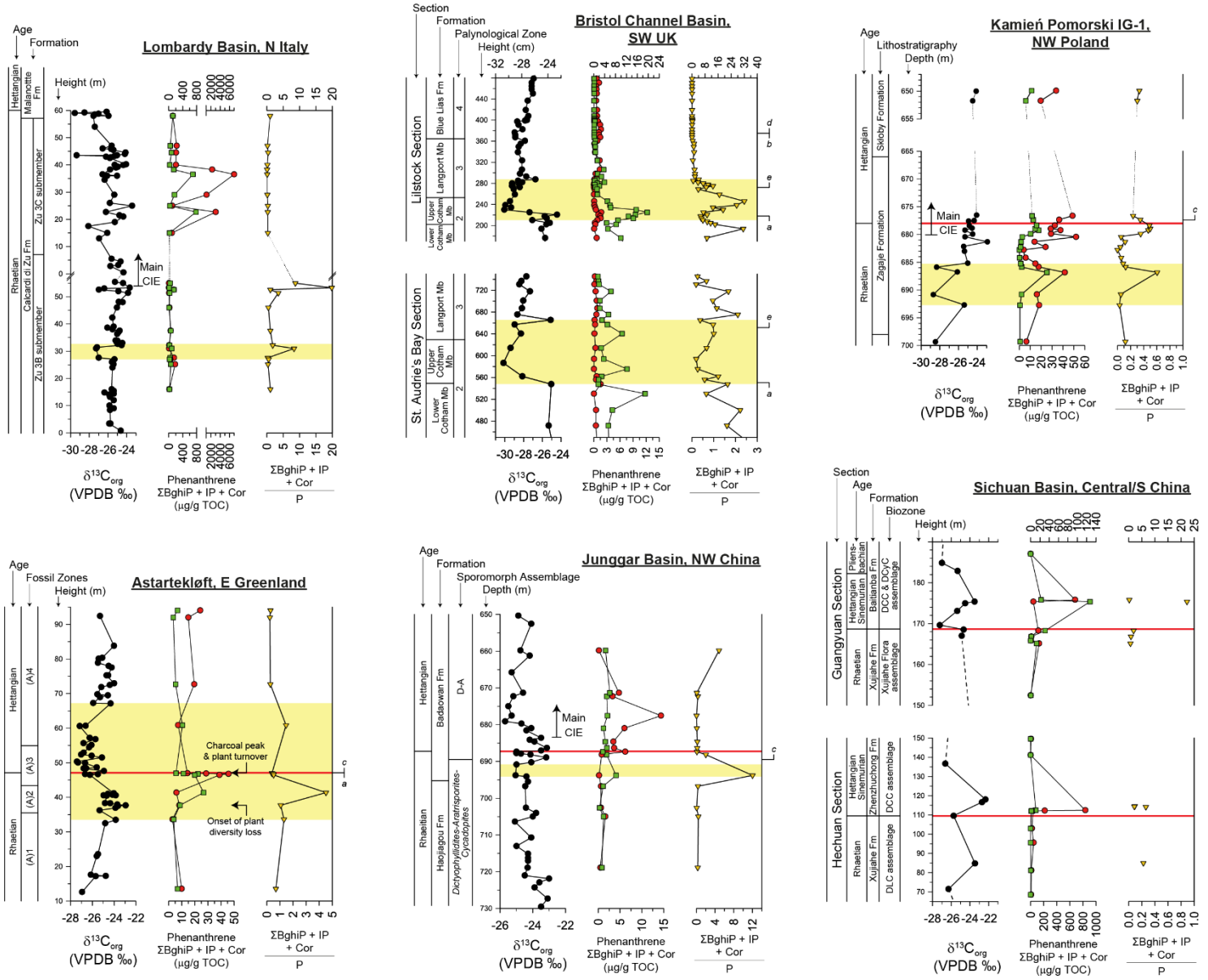
Lombardy Basin, N Italy
Age
Formation
Height (m)
Hettangian
Rhaetian
Malanotte Fm
Calcardi di Zu Fm
Zu 3C submember
Zu 3B submember
Main CIE
δ13Corg (VPDB ‰)
Phenanthrene ΣBghiP + IP + Cor (µg/g TOC)
ΣBghiP + IP + Cor / P
Bristol Channel Basin, SW UK
Section
Formation
Palynological Zone
Height (cm)
Lilstock Section
Blue Lias Fm
Langport Mb
Upper Cotham Mb
Lower Cotham Mb
St. Audrie's Bay Section
Kamień Pomorski IG-1, NW Poland
Lithostratigraphy
Depth (m)
Skloby Formation
Zagaje Formation
Astartekløft, E Greenland
Fossil Zones
(A)1
(A)2
(A)3
(A)4
Charcoal peak & plant turnover
Onset of plant diversity loss
Junggar Basin, NW China
Sporomorph Assemblage
Badaowan Fm
Haojiagou Fm
D-A
Dictyophyllites-Acratisporites-Cycadopites
Sichuan Basin, Central/S China
Biozone
Guangyuan Section
Hettangian-Sinemurian
Rhaetian
Baitianba Fm
Xujiahe Fm
DCC & DCyC assemblage
Xujiahe Flora assemblage
Hechuan Section
Zhenzhuchong Fm
DCC assemblage
DLC assemblage

Fig 6: Comparison of PAH_{PCD} relative to the $\delta^{13}C_{org}$ record across European, Greenland, and Chinese ETE sections. For locations in relation to the CAMP see Fig. 1. Across all sections and in all plots red circles represent phenanthrene (P), green squares represent the sum of benzo[*ghi*]perylene (BghiP), indeno[1,2,3-cd]pyrene (IP) and coronene (Cor), and yellow triangles represent the ratio (BghiP + IP + Cor)/phenanthrene. These PAH_{PCD} were chosen since they were the common compounds measured in all sections. Where present, highlighted yellow areas indicate the initial CIE often used in chemostratigraphic correlations and the red line represents the Triassic-Jurassic boundary. Lombardy Basin PAHs from this study and $\delta^{13}C_{org}$ record from Zaffani et al., (2018). Bristol Channel Basin PAHs from Fox et al., (2022b), $\delta^{13}C_{org}$ record from Fox et al., (2020), and palynological zones and biostratigraphy from Bonis et al., (2010). Kamień Pomorski IG-1 PAHs from Marynowski and Simoneit, (2009) and $\delta^{13}C_{org}$ record and biostratigraphy from Pieńkowski et al., (2011). Astartekløft PAHs from Williford et al., (2014), $\delta^{13}C_{org}$ record from Hesselbo et al., (2002), fossil zones and biostratigraphy from Mander et al., (2013) and McElwain et al., (2009 and refs therein), and charcoal abundance peak after Belcher et al., (2010). Junggar Basin PAHs and $\delta^{13}C_{org}$ record from Zhang et al., (2020) and Fang et al., (2021) and sporomorph assemblage and biostratigraphy from Sha et al., (2015). Sichuan Basin PAHs and $\delta^{13}C_{org}$ record from Song et al., (2020) and biozone from Wang et al., (2010). Note that the Bristol Channel and Sichuan Basins show two sections from their respective basins. Biostratigraphic markers follow those used in correlations of Lindström et al., (2017): a – last common occurrence of *Rhaetogonyaulax rhaetica*; b – last occurrence of *Rhaetogonyaulax rhaetica*; c – first occurrence of *Cerebropollenites thiergartii*; d – first occurrence of *ischyosporites variegatus*; e – *Kraeuselisporites reissingerii*. Fm – Formation. Mb – Member.

5.3: Global records of ETE PAH_{PCD}

In Figure 6, we compare PAH_{PCD} from ETE sections in European, Greenland, and Chinese basins. In these sections, where possible, the initial CIE, Triassic-Jurassic boundary, and occurrences of biostratigraphic markers are identified to help to make comparisons between sections. By comparing the abundances of phenanthrene and the sum of benzo[*ghi*]perylene, indeno[1,2,3-cd]pyrene, and coronene (∑BghiP + IP + Cor), and the ratio of benzo[*ghi*]perylene, indeno[1,2,3-cd]pyrene, and coronene to phenanthrene (BghiP + IP + Cor/P), intensity, duration, and extent of CAMP-driven wildfires can be inferred. In all sections in which the initial CIE is identified, increases in BghiP + IP + Cor/P occur within the initial CIE, with the exception of St. Audrie's Bay (SW, UK). However, many of these increases coincide with low abundances of ∑BghiP + IP + Cor (Lombardy and Bristol Channel basins) or show BghiP + IP + Cor/P values less than 1 (Kamień Pomorski IG-1, St. Audrie's Bay, Guangyuan, and Hechuan sections), suggesting these intervals do not robustly represent intense wildfire activity close to the deposition site as intensive fire would presumably show increased concentrations of ∑BghiP + IP + Cor beyond the background values of phenanthrene. Notably,

there is large differences in both ∑BghiP + IP + Cor and BghiP + IP + Cor/P between St. Audrie's Bay and Lilstock in the Bristol Channel Basin (SW UK). These differences are likely related to a source other than combustion given the extremely close proximity of the sections (~7 km) and evidence of terrestrial input, see Fox et al., (2022b). These records reveal that few of the studied sections show relatively good evidence for more intense biomass burning close to the deposition site during the initial CIE. The best evidence for more intense biomass burning comes from Astartekløft, Greenland and the Junggar Basin, China where increases in BghiP + IP + Cor/P coincide with elevations in ∑BghiP + IP + Cor, perturbations to the organic carbon cycle, the first occurrence of *Cerebropollenites thiergartii*, and loss of plant diversity/plant turnover (Fig. 6). Elevated BghiP + IP + Cor/P ratios are also observed in the Guanguan section, Sichuan Basin, in Hettangian and Sinemurian aged sediments. These increases, although possibly still CAMP-derived due to the duration of peak CAMP activity lasting for less than 1 million years from ca. 201 Ma (Marzoli et al., 2018), are unlikely to be related to the ETE. However, BghiP + IP + Cor/P values comparable with the Astartekløft (Greenland) and Italcementi (Italy) sections (i.e., ~5) are observed just before the Triassic-Jurassic boundary that may be better related to the ETE. Above the initial CIE, in the uppermost Rhaetian and lowermost Hettangian, a common feature across all ETE PAH records presented here are an increase in phenanthrene abundance above the background level with relatively minor increases in the ∑BghiP + IP + Cor. Smoke aerosols that can travel distances of up to ~10,000 km contain abundant LMW PAH_{PCD}, including phenanthrene, and low abundances of HMW PAH_{PCD}, including benzo[*ghi*]perylene and indeno[1,2,3-cd]pyrene (Karp et al., 2020). For context, the distance today between central Greenland and Bolonga, Italy is ~4000 km. Additionally, phenanthrene may represent less intensive paleowildfire activity. Thus, increases in phenanthrene compared to the ∑BghiP + IP + Cor across multiple sections point to smoke signals from possibly more intense fire events further from the deposition site and/or more globally widespread fire events that are of longer duration but less intense than those evidenced later (i.e., older) in the geological record surrounding the time of the initial CIE. This provides evidence of widespread fire activity across multiple basins, corroborated by charcoal abundances (Fig. 1), supporting that wildfire activity was an important terrestrial ecological stressor during the ETE, and that other wildfire associated stressors such as increased toxicity were also important. However, such a hypothesis assumes PAHs derive from combustion sources. To fully explore the widespread fire regime of the ETE and other mass extinction event, future PAH studies need to investigate source of PAHs (pyrogenic vs. petrogenic) as

well as other proxies to help determine fire intensity and smoke versus char/burn residue as exemplified by Song et al., (2020), Kaiho et al., (2022) Fox et al., (2022b) and this study.

6: Conclusions

A comprehensive study of PAH distributions derived from soil-erosion and combustion origins in the Italcementi section, Lombardy Basin, N Italy supports a short-lived but more intense paleowildfire event at a $\delta^{13}C_{org}$ anomaly thought to represent the onset of the main CIE. This event coincides with $CaCO_3$ productivity crisis and onset of a calcareous nannofossil calcification crisis, linking terrestrial and marine ecosystem stresses. Later in the record, abundant PAH_{PCD}, mostly dominated by phenanthrene, support predominant smoke signals and therefore a wildfire event further afield from the deposition site. However, a less intense but more prolonged wildfire activity must also be considered due in increases in LMW and HMW PAH_{PCD} as well as a petrogenic (soil/weathering) source for PAH_{PCD} since PAH ratios suggest a mix of sources. Ratios of phenanthrene and its methylated homologues (APDI scores) suggest that during this event, conifers were the likely source of the burnt material and low abundances of biphenyl, DBT, and DBF compared to PAH_{PCD} support soil erosion activity being a less prominent terrestrial ecosystem stress at this locality. Further, there is limited fire activity and/or massive soil erosion during deposition of the initial CIE routinely used in chemostratigraphic correlations. Comparing the Italcementi section with other ETE sections from Greenland, Europe, and China, PAH distributions from only Greenland and China (Junggar Basin) show evidence of intensive wildfire activity, *albeit* short-lived, during the initial CIE. A feature common across all these sections are increases in phenanthrene in units stratigraphically higher than the initial CIE. These profiles suggest a prominent smoke signal in the latest Rhaetian and earliest Hettangian that could be associated with more intensive paleowildfire events further from the depositional site and/or less intensive wildfire activity at the respective depositional sites. This evidence of fire activity is more widespread and of longer duration compared to those evidenced during the initial CIE. This provides evidence of likely CAMP-driven widespread paleowildfire activity across multiple basins surrounding the time of ETE that were important for terrestrial ecosystem perturbations, but such studies require further investigations to determine e.g., origins of PAHs (pyrogenic *versus* petrogenic) to fully determine the fire history of the ETE.

Acknowledgements

Acknowledgements: We acknowledge Peter Hopper for technical support and Leszek Marynowski, Yi Song, Yanan Fang and Xinzhi Zhang for providing additional PAH data from their respective publications which made possible our global PAH comparisons. **Funding:** Fox acknowledges Curtin University, the European Association of Organic Geochemistry. Fox and Al Suwaidi acknowledge Khalifa University of Science and Technology (CIRA-2019-066). Fox, Holman, and Grice thank the ARC (LP150100341; LE110100119; LE100100041; LE0882836) and The Institute for Geoscience Research. Additional financial support is from the University of Padova DOR2281100/22 to M. Rigo. **Competing interests:** Authors declare no competing interests.

References

Alipour, M., Alizadeh, B., Jahangard, A., GandomiSani, A., 2021. Wildfire events at the Triassic–Jurassic boundary of the Tabas Basin, Central Iran. Int. J. Coal Sci. Technol. 8, 897–907. https://doi.org/10.1007/s40789-021-00436-2

Arias, A.H., Souissi, A., Glippa, O., Roussin, M., Dumoulin, D., Net, S., Ouddane, B., Souissi, S., 2017. Removal and Biodegradation of Phenanthrene, Fluoranthene and Pyrene by the Marine Algae Rhodomonas baltica Enriched from North Atlantic Coasts. Bull. Environ. Contam. Toxicol. 98, 392–399. https://doi.org/10.1007/s00128-016-1967-4

Atkinson, J.W., Wignall, P.B., 2019. How quick was marine recovery after the end-Triassic mass extinction and what role did anoxia play? Palaeogeogr. Palaeoclimatol. Palaeoecol. 528, 99–119. https://doi.org/https://doi.org/10.1016/j.palaeo.2019.05.011

Baker, S.J., 2022. Fossil evidence that increased wildfire activity occurs in tandem with periods of global warming in Earth's past. Earth-Science Rev. 224, 103871. https://doi.org/https://doi.org/10.1016/j.earscirev.2021.103871

Beaulieu, J.M., O'Meara, B.C., Crane, P., Donoghue, M.J., 2015. Heterogeneous Rates of Molecular Evolution and Diversification Could Explain the Triassic Age Estimate for Angiosperms. Syst. Biol. 64, 869–878. https://doi.org/10.1093/sysbio/syv027

Beith, S.J., Fox, C.P., Marshall, J.E.A., Whiteside, J.H., 2021. Recurring photic zone euxinia

748 in the nrthwest Tethys impinged end-Triassic recovery. Palaeogeogr. Palaeoclimatol.
749 Palaeoecol. (in Press. 584, 110680.
750 https://doi.org/https://doi.org/10.1016/j.palaeo.2021.110680

751 Belcher, C.M., Mander, L., Rein, G., Jervis, F.X., Haworth, M., Hesselbo, S.P., Glasspool,
752 I.J., McElwain, J.C., 2010. Increased fire activity at the Triassic/Jurassic boundary in
753 Greenland due to climate-driven floral change. Nat. Geosci. 3, 426–429.
754 https://doi.org/10.1038/ngeo871

755 Bennett, B., Larter, S.R., 2008. Biodegradation scales: Applications and limitations. Org.
756 Geochem. 39, 1222–1228.
757 https://doi.org/https://doi.org/10.1016/j.orggeochem.2008.02.023

758 Blackburn, T.J., Olsen, P.E., Bowring, S.A., McLean, N.M., Kent, D. V., Puffer, J., McHone,
759 G., Rasbury, E.T., Mohammed, E.-T., 2013. Zircon U-Pb Geochronology Links the End-
760 Triassic Extinction with the Central Atlantic Magmatic Province. Science (80-.). 340,
761 941–945. https://doi.org/10.1126/science.1234204

762 Bond, A.D., Dickson, A.J., Ruhl, M., Raine, R., 2022. Marine redox change and extinction in
763 Triassic–Jurassic boundary strata from the Larne Basin, Northern Ireland. Palaeogeogr.
764 Palaeoclimatol. Palaeoecol. 598, 111018.
765 https://doi.org/https://doi.org/10.1016/j.palaeo.2022.111018

766 Bonis, N.R., Ruhl, M., Kürschner, W.M., 2010. Milankovitch-scale palynological turnover
767 across the Triassic–Jurassic transition at St. Audrie's Bay, SW UK. J. Geol. Soc.
768 London. 167, 877–888. https://doi.org/10.1144/0016-76492009-141

769 Bottini, C., Jadoul, F., Rigo, M., Zaffani, M., Artoni, C., Erba, E., 2016. Calcareous
770 nannofossils at the Triassic/Jurassic boundary: stratigraphic and paleoceanographic
771 characterization. Riv. Ital. di Paleontol. e Stratigr. 122, 141–164.
772 https://doi.org/https://doi.org/10.13130/2039-4942/7726

773 Boudinot, F.G., Sepúlveda, J., 2020. Marine organic carbon burial increased forest fire
774 frequency during Oceanic Anoxic Event 2. Nat. Geosci. 13, 693–698.
775 https://doi.org/10.1038/s41561-020-0633-y

776 Cassani, F., Gallango, O., Talukdar, S., Vallejos, C., Ehrmann, U., 1988.
777 Methylphenanthrene maturity index of marine source rock extracts and crude oils from

778 the Maracaibo Basin. Org. Geochem. 13, 73–80.
779 https://doi.org/https://doi.org/10.1016/0146-6380(88)90027-7

780 Coiffard, C., Gomez, B., Daviero-Gomez, V., Dilcher, D.L., 2012. Rise to dominance of
781 angiosperm pioneers in European Cretaceous environments. Proc. Natl. Acad. Sci. 109,
782 20955–20959. https://doi.org/10.1073/pnas.1218633110

783 Cranwell, P.A., Eglinton, G., Robinson, N., 1987. Lipids of aquatic organisms as potential
784 contributors to lacustrine sediments—II. Org. Geochem. 11, 513–527.
785 https://doi.org/https://doi.org/10.1016/0146-6380(87)90007-6

786 Davies, J.H.F.L., Marzoli, A., Bertrand, H., Youbi, N., Ernesto, M., Schaltegger, U., 2017.
787 End-Triassic mass extinction started by intrusive CAMP activity. Nat. Commun. 8,
788 15596. https://doi.org/10.1038/ncomms15596

789 Denis, E.H., Maibauer, B.J., Bowen, G.J., Jardine, P.E., Harrington, G.J., Baczynski, A.A.,
790 McInerney, F.A., Collinson, M.E., Belcher, C.M., Wing, S.L., Freeman, K.H., 2021.
791 Decreased soil carbon in a warming world: Degraded pyrogenic carbon during the
792 Paleocene-Eocene Thermal Maximum, Bighorn Basin, Wyoming. Earth Planet. Sci.
793 Lett. 566, 116970. https://doi.org/https://doi.org/10.1016/j.epsl.2021.116970

794 Du, Y., Chiari, M., Karádi, V., Nicora, A., Onoue, T., Pálfy, J., Roghi, G., Tomimatsu, Y.,
795 Rigo, M., 2020. The asynchronous disappearance of conodonts: New constraints from
796 Triassic-Jurassic boundary sections in the Tethys and Panthalassa. Earth-Science Rev.
797 203, 103176. https://doi.org/https://doi.org/10.1016/j.earscirev.2020.103176

798 Eglinton, G., Gonzalez, A.G., Hamilton, R.J., Raphael, R.A., 1962. Hydrocarbon constituents
799 of the wax coatings of plant leaves: A taxonomic survey. Phytochemistry 1, 89–102.
800 https://doi.org/https://doi.org/10.1016/S0031-9422(00)88006-1

801 Fang, Y., Fang, L., Deng, S., Lu, Y., Wang, B., Zhao, X., Wang, Y., Zhang, H., Zhang, X.,
802 Sha, J., 2021. Carbon isotope stratigraphy across the Triassic-Jurassic boundary in the
803 high-latitude terrestrial Junggar Basin, NW China. Palaeogeogr. Palaeoclimatol.
804 Palaeoecol. 577, 110559. https://doi.org/https://doi.org/10.1016/j.palaeo.2021.110559

805 Fenton, S., Grice, K., Twitchett, R.J., Böttcher, M.E., Looy, C. V, Nabbefeld, B., 2007.
806 Changes in biomarker abundances and sulfur isotopes of pyrite across the Permian–
807 Triassic (P/Tr) Schuchert Dal section (East Greenland). Earth Planet. Sci. Lett. 262,

230–239. https://doi.org/https://doi.org/10.1016/j.epsl.2007.07.033

Finkelstein, D.B., Pratt, L.M., Curtin, T.M., Brassell, S.C., 2005. Wildfires and seasonal aridity recorded in Late Cretaceous strata from south-eastern Arizona, USA. Sedimentology 52, 587–599. https://doi.org/https://doi.org/10.1111/j.1365-3091.2005.00712.x

Fox, C.P., Cui, X., Whiteside, J.H., Olsen, P.E., Summons, R.E., Grice, K., 2020. Molecular and isotopic evidence reveals the end-Triassic carbon isotope excursion is not from massive exogenous light carbon. Proc. Natl. Acad. Sci. 117, 30171 LP – 30178. https://doi.org/10.1073/pnas.1917661117

Fox, C.P., Whiteside, J.H., Olsen, P.E., Cui, X., Summons, R.E., Idiz, E., Grice, K., 2022a. Two-pronged kill mechanism at the end-Triassic mass extinction. Geology. https://doi.org/10.1130/G49560.1

Fox, C.P., Whiteside, J.H., Olsen, P.E., Grice, K., 2022b. Flame out! End-Triassic mass extinction polycyclic aromatic hydrocarbons reflect more than just fire. Earth Planet. Sci. Lett. in press.

Fujisaki, W., Matsui, Y., Asanuma, H., Sawaki, Y., Suzuki, K., Maruyama, S., 2018. Global perturbations of carbon cycle during the Triassic–Jurassic transition recorded in the mid-Panthalassa. Earth Planet. Sci. Lett. 500, 105–116. https://doi.org/https://doi.org/10.1016/j.epsl.2018.07.026

Galli, M.T., Jadoul, F., Bernasconi, S.M., Cirilli, S., Weissert, H., 2007. Stratigraphy and palaeoenvironmental analysis of the Triassic–Jurassic transition in the western Southern Alps (Northern Italy). Palaeogeogr. Palaeoclimatol. Palaeoecol. 244, 52–70. https://doi.org/https://doi.org/10.1016/j.palaeo.2006.06.023

Grice, K., Backhouse, J., Alexander, R., Marshall, N., Logan, G.A., 2005. Correlating terrestrial signatures from biomarker distributions, δ13C, and palynology in fluvio-deltaic deposits from NW Australia (Triassic–Jurassic). Org. Geochem. 36, 1347–1358. https://doi.org/https://doi.org/10.1016/j.orggeochem.2005.06.003

Grice, K., Nabbefeld, B., Maslen, E., 2007. Source and significance of selected polycyclic aromatic hydrocarbons in sediments (Hovea-3 well, Perth Basin, Western Australia) spanning the Permian–Triassic boundary. Org. Geochem. 38, 1795–1803.

https://doi.org/https://doi.org/10.1016/j.orggeochem.2007.07.001

Gulick, Sean P S, Bralower, T.J., Ormö, J., Hall, B., Grice, K., Schaefer, B., Lyons, S., Freeman, K.H., Morgan, Joanna V, Artemieva, N., Kaskes, P., de Graaff, S.J., Whalen, Michael T, Collins, G.S., Tikoo, Sonia M, Verhagen, C., Christeson, Gail L, Claeys, Philippe, Coolen, Marco J L, Goderis, S., Goto, Kazuhisa, Grieve, R.A.F., McCall, N., Osinski, G.R., Rae, Auriol S P, Riller, Ulrich, Smit, Jan, Vajda, V., Wittmann, Axel, Null, N., Gulick, S P S, Morgan, J V, Bralower, T., Cheno, E., Christeson, G L, Claeys, P, Cockell, C.S., Coolen, M J L, Ferrière, L., Gebhardt, C., Goto, K, Green, S., Jones, H., Kring, D.A., LeBer, E., Lofi, J., Lowery, C.M., OcampoTorres, R., Cruz, L.P., Pickersgill, A.E., Poelchau, M.H., Rae, A S P, Rasmussen, C., Vieyra, M.R., Riller, U, Sato, H., Schmitt, D., Smit, J, Tikoo, S M, Tomioka, N., Fucugauchi, J.U., Whalen, M T, Wittmann, A, Xiao, L., Yamaguchi, K.E., 2019. The first day of the Cenozoic. Proc. Natl. Acad. Sci. 116, 19342–19351. https://doi.org/10.1073/pnas.1909479116

Harris, T.M., 1958. Forest Fire in the Mesozoic. J. Ecol. 46, 447–453. https://doi.org/10.2307/2257405

He, T., Dal Corso, J., Newton, R.J., Wignall, P.B., Mills, B.J.W., Todaro, S., Di Stefano, P., Turner, E.C., Jamieson, R.A., Randazzo, V., Rigo, M., Jones, R.E., Dunhill, A.M., 2020. An enormous sulfur isotope excursion indicates marine anoxia during the end-Triassic mass extinction. Sci. Adv. 6. https://doi.org/10.1126/sciadv.abb6704

He, T., Wignall, P.B., Newton, R.J., Atkinson, J.W., Keeling, J.F.J., Xiong, Y., Poulton, S.W., 2022. Extensive marine anoxia in the European epicontinental sea during the end-Triassic mass extinction. Glob. Planet. Change 210, 103771. https://doi.org/https://doi.org/10.1016/j.gloplacha.2022.103771

Hesselbo, S.P., Robinson, S.A., Surlyk, F., Piasecki, S., 2002. Terrestrial and marine extinction at the Triassic-Jurassic boundary synchronized with major carbon-cycle perturbation: A link to initiation of massive volcanism? Geology 30, 251–254.

Holman, A.I., Grice, K., 2018. $\delta^{13}C$ of aromatic compounds in sediments, oils and atmospheric emissions: A review. Org. Geochem. 123, 27–37. https://doi.org/https://doi.org/10.1016/j.orggeochem.2018.06.004

Holman, A.I., Grice, K., Jaraula, C.M.B., Schimmelmann, A., 2014. Bitumen II from the Paleoproterozoic Here's Your Chance Pb/Zn/Ag deposit: Implications for the analysis of

depositional environment and thermal maturity of hydrothermally-altered sediments. Geochim. Cosmochim. Acta 139, 98–109. https://doi.org/https://doi.org/10.1016/j.gca.2014.04.035

Jadoul, F., Galli, M.T., 2008. The Hettangian shallow water carbonates after the Triassic/Jurassic biocalcification crisis: The Albenza Formation in the Western Southern Alps. Riv. Ital. di Paleontol. e Stratigr. 114, 453–470. https://doi.org/https://doi.org/10.13130/2039-4942/5911

Jadoul, F., Galli, M.T., Berra, F., Cirilli, S., Ronchi, P., Paganoni, A.M., 2004. The Late Triassic-Early Jurassic of the Lombardy Basin: stratigraphy, palaeogeography and palaeontology. Field guide book escursion P86.

Jadoul, F., Galli, M.T., Muttoni, G., Rigo, M., Cirilli, S., 2007. The late Norian-Hettangian stratigraphic and paleogeographic evolution of the Bergamasc Alps. Geoitalia, VI FIST Meet. 4, 1–55. https://doi.org/10.3301 / GFT.2012.01

Jadoul, F., Masetti, D., Cirilli, S., Berra, F., Claps, M., Frisia, S., 1994. Norian–Rhaetian stratigraphy and paleogeographic evolution of the Lombardy Basin (Bergamasc Alps), in: 15th IAS Regional Meeting. pp. 5–38.

Jaraula, C.M.B., Grice, K., Twitchett, R.J., Böttcher, M.E., LeMetayer, P., Dastidar, A.G., Opazo, L.F., 2013. Elevated pCO_2 leading to Late Triassic extinction, persistent photic zone euxinia, and rising sea levels. Geology 41, 955–958. https://doi.org/10.1130/G34183.1

Kaiho, K., Aftabuzzaman, M., Jones, D.S., Tian, L., 2020. Pulsed volcanic combustion events coincident with the end-Permian terrestrial disturbance and the following global crisis. Geology 49, 289–293. https://doi.org/10.1130/G48022.1

Kaiho, K., Saito, R., Ito, K., Miyaji, T., Biswas, R., Tian, L., Sano, H., Shi, Z., Takahashi, S., Tong, J., Liang, L., Oba, M., Nara, F.W., Tsuchiya, N., Chen, Z.-Q., 2016. Effects of soil erosion and anoxic–euxinic ocean in the Permian–Triassic marine crisis. Heliyon 2, e00137. https://doi.org/https://doi.org/10.1016/j.heliyon.2016.e00137

Kaiho, K., Tanaka, D., Richoz, S., Jones, D.S., Saito, R., Kameyama, D., Ikeda, M., Takahashi, S., Aftabuzzaman, M., Fujibayashi, M., 2022. Volcanic temperature changes modulated volatile release and climate fluctuations at the end-Triassic mass extinction.

899 Earth Planet. Sci. Lett. 579, 117364.
900 https://doi.org/https://doi.org/10.1016/j.epsl.2021.117364

901 Kaiho, K., Yatsu, S., Oba, M., Gorjan, P., Casier, J.-G., Ikeda, M., 2013. A forest fire and soil
902 erosion event during the Late Devonian mass extinction. Palaeogeogr. Palaeoclimatol.
903 Palaeoecol. 392, 272–280. https://doi.org/https://doi.org/10.1016/j.palaeo.2013.09.008

904 Kappenberg, A., Braun, M., Amelung, W., Lehndorff, E., 2019. Fire condensates and
905 charcoals: Chemical composition and fuel source identification. Org. Geochem. 130,
906 43–50. https://doi.org/https://doi.org/10.1016/j.orggeochem.2019.01.009

907 Karp, A.T., Behrensmeyer, A.K., Freeman, K.H., 2018. Grassland fire ecology has roots in
908 the late Miocene. Proc. Natl. Acad. Sci. 115, 12130 LP – 12135.
909 https://doi.org/10.1073/pnas.1809758115

910 Karp, A.T., Holman, A.I., Hopper, P., Grice, K., Freeman, K.H., 2020. Fire distinguishers:
911 Refined interpretations of polycyclic aromatic hydrocarbons for paleo-applications.
912 Geochim. Cosmochim. Acta 289, 93–113.
913 https://doi.org/https://doi.org/10.1016/j.gca.2020.08.024

914 Kasprak, A.H., Sepúlveda, J., Price-Waldman, R., Williford, K.H., Schoepfer, S.D., Haggart,
915 J.W., Ward, P.D., Summons, R.E., Whiteside, J.H., 2015. Episodic photic zone euxinia
916 in the northeastern Panthalassic Ocean during the end-Triassic extinction. Geology 43,
917 307–310. https://doi.org/10.1130/G36371.1

918 Kent, D. V, Muttoni, G., 2003. Mobility of Pangea: implications for Late Paleozoic and early
919 Mesozoic paleoclimate, in: LeTourneau, P.M., Olsen, P.E. (Eds.), Great Rift Valleys of
920 Pangea in Eastern North America, Tectonics, Structure, and Volcanism, Vol. 1.
921 Columbia University Press, pp. 12–20.

922 Lakew, T., 1990. Microfacies and cyclic sedimentation of the Upper Triassic (Rhaetian)
923 Calcare di Zu (Southern Alps). Facies 22, 187–231. https://doi.org/10.1007/bf02536952

924 Lindström, S., Callegaro, S., Davies, J., Tegner, C., van de Schootbrugge, B., Pedersen, G.K.,
925 Youbi, N., Sanei, H., Marzoli, A., 2021. Tracing volcanic emissions from the Central
926 Atlantic Magmatic Province in the sedimentary record. Earth-Science Rev. 212, 103444.
927 https://doi.org/https://doi.org/10.1016/j.earscirev.2020.103444

928 Lindström, S., Sanei, H., van de Schootbrugge, B., Pedersen, G.K., Lesher, C.E., Tegner, C.,

Heunisch, C., Dybkjær, K., Outridge, P.M., 2019. Volcanic mercury and mutagenesis in land plants during the end-Triassic mass extinction. Sci. Adv. 5, eaaw4018. https://doi.org/10.1126/sciadv.aaw4018

Lindström, S., van de Schootbrugge, B., Hansen, K.H., Pedersen, G.K., Alsen, P., Thibault, N., Dybkjær, K., Bjerrum, C.J., Nielsen, L.H., 2017. A new correlation of Triassic–Jurassic boundary successions in NW Europe, Nevada and Peru, and the Central Atlantic Magmatic Province: A time-line for the end-Triassic mass extinction. Palaeogeogr. Palaeoclimatol. Palaeoecol. 478, 80–102. https://doi.org/https://doi.org/10.1016/j.palaeo.2016.12.025

Lyons, S.L., Karp, A.T., Bralower, T.J., Grice, K., Schaefer, B., Gulick, S.P.S., Morgan, J. V, Freeman, K.H., 2020. Organic matter from the Chicxulub crater exacerbated the K–Pg impact winter. Proc. Natl. Acad. Sci. 117, 25327–25334. https://doi.org/10.1073/pnas.2004596117

Mander, L., Kürschner, W.M., McElwain, J.C., 2013. Palynostratigraphy and vegetation history of the Triassic{\textendash}Jurassic transition in East Greenland. J. Geol. Soc. London. 170, 37–46. https://doi.org/10.1144/jgs2012-018

Marynowski, L., Simoneit, B.R.T., 2009. Widespread upper Triassic to lower Jurassic wildfire records from Poland: Evidence from charcoal and pyrolytic and pyrolytic polycyclic aromatic hydrocarbons. Palaios 24, 785–798.

Marzoli, A., Callegaro, S., Dal Corso, J., Davies, J.H.F.L., Chiaradia, M., Youbi, N., Bertrand, H., Reisberg, L., Merle, R., Jourdan, F., 2018. The Central Atlantic Magmatic Province (CAMP): A Review, in: Tanner, L.H. (Ed.), The Late Triassic World: Earth in a Time of Transition. Springer International Publishing, Cham, pp. 91–125. https://doi.org/10.1007/978-3-319-68009-5_4

McElwain, J.C., Beerling, D, J., Woodward F. I., 1999. Fossil Plants and Global Warming at the Triassic-Jurassic Boundary. Science (80-.). 285, 1386–1390. https://doi.org/10.1126/science.285.5432.1386

McElwain, J.C., Wagner, P.J., Hesselbo, S.P., 2009. Fossil Plant Relative Abundances Indicate Sudden Loss of Late Triassic Biodiversity in East Greenland. Science (80-.). 324, 1554–1556. https://doi.org/10.1126/science.1171706

McKay, D.S., Gibson, E.K., Thomas-Keprta, K.L., Vali, H., Romanek, C.S., Clemett, S.J., Chillier, X.D.F., Maechling, C.R., Zare, R.N., 1996. Search for Past Life on Mars: Possible Relic Biogenic Activity in Martian Meteorite ALH84001. Science (80-.). 273, 924–930.

McRoberts, C., 2008. Rhaetian bivalves and the Norian/Rhaetian boundary, in: Krystyn, L., Mandl, G.W. (Eds.), Upper Triassic Subdivision, Zonations and Events. Berichte der Geologischen Bundesanstalt, 76, pp. 41–44.

McRoberts, C.A., Krystyn, L., Hautmann, M., 2012. Macrofaunal response to the end-Triasic mass extinction in the west-Tethyan Kössen Basin, Austria. Paliaos 27, 608–617.

Muttoni, G., Kent, D. V, Jadoul, F., Olsen, P.E., Rigo, M., Galli, M.T., Nicora, A., 2010. Rhaetian magneto-biostratigraphy from the Southern Alps (Italy): Constraints on Triassic chronology. Palaeogeogr. Palaeoclimatol. Palaeoecol. 285, 1–16. https://doi.org/https://doi.org/10.1016/j.palaeo.2009.10.014

Nabbefeld, B., Grice, K., Summons, R.E., Hays, L.E., Cao, C., 2010. Significance of polycyclic aromatic hydrocarbons (PAHs) in Permian/Triassic boundary sections. Appl. Geochemistry 25, 1374–1382. https://doi.org/https://doi.org/10.1016/j.apgeochem.2010.06.008

Pálfy, J., 2003. Volcanism of the Central Atlantic Magmatic Province as a potential driving force in the end-Triassic mass extinction. Cent. Atl. Magmat. Prov. Geophys. Monogr. Ser. 136, 255–267. https://doi.org/10.1029/136GM014

Peters, K.E., Walters, C.C., Moldowan, J.M., 2004. The Biomarker Guide: Volume 1: Biomarkers and Isotopes in the Environment and Human History, 2nd ed. Cambridge University Press, Cambridge. https://doi.org/DOI: 10.1017/CBO9780511524868

Petersen, H.I., Lindström, S., 2012. Synchronous Wildfire Activity Rise and Mire Deforestation at the Triassic–Jurassic Boundary. PLoS One 7, e47236.

Philp, R.P., DeGarmo, C.D., 2020. Geochemical characterization of the Devonian-Mississippian Woodford Shale from the McAlister Cemetery Quarry, Criner Hills Uplift, Ardmore Basin, Oklahoma. Mar. Pet. Geol. 112, 104078. https://doi.org/https://doi.org/10.1016/j.marpetgeo.2019.104078

Pieńkowski, G., Niedźwiedzki, G., Waksmundzka, M., 2011. Sedimentological,

989 palynological and geochemical studies of the terrestrial Triassic–Jurassic boundary in
990 northwestern Poland. Geol. Mag. 149, 308–332.
991 https://doi.org/10.1017/S0016756811000914

992 Pole, M., Wang, Y., Dong, C., Xie, X., Tian, N., Li, L., Zhou, N., Lu, N., Xie, A., Zhang, X.,
993 2018. Fires and storms—a Triassic–Jurassic transition section in the Sichuan Basin,
994 China. Palaeobiodiversity and Palaeoenvironments 98, 29–47.
995 https://doi.org/10.1007/s12549-017-0315-y

996 Ramdahl, T., 1983. Retene—a molecular marker of wood combustion in ambient air. Nature
997 306, 580–582. https://doi.org/10.1038/306580a0

998 Romero-Sarmiento, M.-F., Riboulleau, A., Vecoli, M., Versteegh, G.J.M., 2010. Occurrence
999 of retene in upper Silurian–lower Devonian sediments from North Africa: Origin and
1000 implications. Org. Geochem. 41, 302–306.
1001 https://doi.org/https://doi.org/10.1016/j.orggeochem.2009.10.003

1002 Schoene, B., Guex, J., Bartolini, A., Schaltegger, U., Blackburn, T.J., 2010. Correlating the
1003 end-Triassic mass extinction and flood basalt volcanism at the 100 ka level. Geology 38,
1004 387–390. https://doi.org/10.1130/G30683.1

1005 Sephton, M.A., Looy, C. V, Brinkhuis, H., Wignall, P.B., de Leeuw, J.W., Visscher, H.,
1006 2005. Catastrophic soil erosion during the end-Permian biotic crisis. Geology 33, 941–
1007 944. https://doi.org/10.1130/G21784.1

1008 Sepkoski, J.J., 1993. Ten Years in the Library: New Data Confirm Paleontological Patterns.
1009 Paleobiology 19, 43–51.

1010 Sha, J., Olsen, P.E., Pan, Y., Xu, D., Wang, Y., Zhang, X., Yao, X., Vajda, V., 2015.
1011 Triassic–Jurassic climate in continental high-latitude Asia was dominated by obliquity-
1012 paced variations (Junggar Basin, Ürümqi, China). Proc. Natl. Acad. Sci. 112, 3624 LP –
1013 3629. https://doi.org/10.1073/pnas.1501137112

1014 Shen, G., Tao, S., Wei, S., Zhang, Y., Wang, R., Wang, B., Li, W., Shen, H., Huang, Y.,
1015 Yang, Y., Wang, W., Wang, X., Simonich, S.L.M., 2012. Retene Emission from
1016 Residential Solid Fuels in China and Evaluation of Retene as a Unique Marker for Soft
1017 Wood Combustion. Environ. Sci. Technol. 46, 4666–4672.
1018 https://doi.org/10.1021/es300144m

1019 Shen, W., Sun, Y., Lin, Y., Liu, D., Chai, P., 2011. Evidence for wildfire in the Meishan
1020 section and implications for Permian–Triassic events. Geochim. Cosmochim. Acta 75,
1021 1992–2006. https://doi.org/https://doi.org/10.1016/j.gca.2011.01.027

1022 Simoneit, B.R.T., Brault, M., Saliot, A., 1990. Hydrocarbons associated with hydrothermal
1023 minerals, vent waters and talus on the East Pacific Rise and Mid-Atlantic Ridge. Appl.
1024 Geochemistry 5, 115–124. https://doi.org/https://doi.org/10.1016/0883-2927(90)90042-4

1025 Song, Y., Algeo, T.J., Wu, W., Luo, G., Li, L., Wang, Y., Xie, S., 2020. Distribution of
1026 pyrolytic PAHs across the Triassic-Jurassic boundary in the Sichuan Basin,
1027 southwestern China: Evidence of wildfire outside the Central Atlantic Magmatic
1028 Province. Earth-Science Rev. 201, 102970.
1029 https://doi.org/https://doi.org/10.1016/j.earscirev.2019.102970

1030 Steinthorsdottir, M., Jeram, A.J., McElwain, J.C., 2011. Extremely elevated CO2
1031 concentrations at the Triassic/Jurassic boundary. Palaeogeogr. Palaeoclimatol.
1032 Palaeoecol. 308, 418–432. https://doi.org/https://doi.org/10.1016/j.palaeo.2011.05.050

1033 Stogiannidis, E., Laane, R., 2015. Source Characterization of Polycyclic Aromatic
1034 Hydrocarbons by Using Their Molecular Indices: An Overview of Possibilities, in:
1035 Whitacre, D.M. (Ed.), Reviews of Environmental Contamination and Toxicology (Vol
1036 234). Springer, pp. 49–133. https://doi.org/10.1007/978-3-319-10638-0

1037 Tegner, C., Marzoli, A., McDonald, I., Youbi, N., Lindström, S., 2020. Platinum-group
1038 elements link the end-Triassic mass extinction and the Central Atlantic Magmatic
1039 Province. Sci. Rep. 10, 3482. https://doi.org/10.1038/s41598-020-60483-8

1040 Uhl, D., Montenari, M., 2011. Charcoal as evidence of palaeo-wildfires in the Late Triassic
1041 of SW Germany. Geol. J. 46, 34–41. https://doi.org/https://doi.org/10.1002/gj.1229

1042 van de Schootbrugge, B., Bachan, A., Suan, G., Richoz, S., Payne, J.L., 2013. Microbes, mud
1043 and methane: cause and consequence of recurrent Early Jurassic anoxia following the
1044 end-Triassic mass extinction. Palaeontology 56, 685–709.
1045 https://doi.org/https://doi.org/10.1111/pala.12034

1046 van de Schootbrugge, B., Quan, T.M., Lindström, S., Püttmann, W., Heunisch, C., Pross, J.,
1047 Fiebig, J., Petschick, R., Röhling, H.-G., Richoz, S., Rosenthal, Y., Falkowski, P.G.,
1048 2009. Floral changes across the Triassic/Jurassic boundary linked to flood basalt

volcanism. Nat. Geosci. 2, 589–594. https://doi.org/10.1038/ngeo577

van de Schootbrugge, B., van der Weijst, C.M.H., Hollaar, T.P., Vecoli, M., Strother, P.K., Kuhlmann, N., Thein, J., Visscher, H., van Konijnenburg-van Cittert, H., Schobben, M.A.N., Sluijs, A., Lindström, S., 2020. Catastrophic soil loss associated with end-Triassic deforestation. Earth-Science Rev. 210, 103332. https://doi.org/10.1016/j.earscirev.2020.103332

van de Schootbrugge, B., Wignall, P.B., 2015. A tale of two extinctions: converging end-Permian and end-Triassic scenarios. Geol. Mag. 153, 332–354. https://doi.org/10.1017/S0016756815000643

Wang, C., Visscher, H., 2007. Abundance anomalies of aromatic biomarkers in the Permian–Triassic boundary section at Meishan, China — Evidence of end-Permian terrestrial ecosystem collapse. Palaeogeogr. Palaeoclimatol. Palaeoecol. 252, 291–303. https://doi.org/https://doi.org/10.1016/j.palaeo.2006.11.048

Wang, Y., Bh, F., Xp, X., Qs, H., Li, K.J., Li, G., Zs, L., Jx, Y., Yh, P., Tian, N., Zk, J., 2010. The terrestrial Triassic and Jurassic Systems in the Sichuan Basin, China. Univ. Sci. Technol. China Press. Hefei, China 216.

Wen, Z., Ruiyong, W., Radke, M., Qingyu, W., Guoying, S., Zhili, L., 2000. Retene in pyrolysates of algal and bacterial organic matter. Org. Geochem. 31, 757–762. https://doi.org/https://doi.org/10.1016/S0146-6380(00)00064-4

Whiteside, J.H., Olsen, P.E., Eglinton, T., Brookfield, M.E., Sambrotto, R.N., 2010. Compound-specific carbon isotopes from Earth's largest flood basalt eruptions directly linked to the end-Triassic mass extinction. Proc. Natl. Acad. Sci. https://doi.org/10.1073/pnas.1001706107

Wignall, P.B., Atkinson, J.W., 2020. A two-phase end-Triassic mass extinction. Earth-Science Rev. 208, 103282. https://doi.org/10.1016/j.earscirev.2020.103282

Williford, K.H., Grice, K., Holman, A., McElwain, J.C., 2014. An organic record of terrestrial ecosystem collapse and recovery at the Triassic–Jurassic boundary in East Greenland. Geochim. Cosmochim. Acta 127, 251–263. https://doi.org/https://doi.org/10.1016/j.gca.2013.11.033

Yunker, M.B., Macdonald, R.W., Vingarzan, R., Mitchell, R.H., Goyette, D., Sylvestre, S.,

2002. PAHs in the Fraser River basin: a critical appraisal of PAH ratios as indicators of PAH source and composition. Org. Geochem. 33, 489–515. https://doi.org/https://doi.org/10.1016/S0146-6380(02)00002-5

Zaffani, M., Jadoul, F., Rigo, M., 2018. A new Rhaetian δ13Corg record: Carbon cycle disturbances, volcanism, End-Triassic mass Extinction (ETE). Earth-Science Rev. 178, 92–104. https://doi.org/https://doi.org/10.1016/j.earscirev.2018.01.004

Zhang, X., Lv, P., Fang, L., Yang, H., Deng, S., Lu, Y., Fang, Y., Zhang, X., Huang, R., Liang, J., Shi, S., 2020. Widefire records across the Triassic-Jurassic boundary in the southern margin of the Junggar Basin and global correlations. Acta Sedimentol. Sin. https://doi.org/10.14027/j.issn.1000-0550.2020.103